Electronic Supplementary Material (ESI) for Chemical Science.

Supplementary Information for

Anti-Arrhenius Behavior of Charge Recombination in Molecular Dimers

Neo Lin[1] and Tomoyasu Mani[1,2]*

[1] Department of Chemistry, University of Connecticut, Storrs CT 06269, United States

[2] Chemistry Division, Brookhaven National Laboratory, Upton NY 11973, United States

* tomoyasu.mani@uconn.edu / tmani@bnl.gov

Table of Contents

1. Experimental

1.1. General Information

All reagents and solvents were sourced from standard commercial chemical supply companies, unless noted otherwise. Silica gel (pore size 60 Å, 230–400 mesh, SiliCycle Inc.) was used in manual flash column chromatography. The ^{1}H and ^{13}C NMR spectra were recorded via a Bruker Avance III spectrometer, operating at 400 and 100 MHz, respectively, or via a Bruker Avance spectrometer, operating at 300 and 75 MHz, respectively. The mass spectra were obtained via QStar Elite (AB Sciex) conducted at the Laboratory of Mass Spectrometry and Omics Analysis of the University of Connecticut Department of Chemistry. UV-vis absorption spectra were recorded by a Cary 50 Scan UV-vis spectrophotometer (Varian). A FLS1000 photoluminescence spectrometer (Edinburgh Instruments) was used to record the steady-state and time-resolved emission. Fluorescence lifetime measurements were performed using a TCSPC system of the FLS1000 equipped with a TCSPC/MCS/counter module (TCC2), a Hamamatsu H10720-01P, and a pulsed diode laser (EPL-510) as the excitation source that provided 506 nm excitation having a pulse duration 85 ps. Global lifetime analysis with instrument response function (IRF) was performed with Fluorescence Analysis Software Technology (FAST, Edinburgh Instruments). Using the FLS1000 equipped with an integrating sphere, absolute measurements were conducted to obtain quantum yields of emission (Φ_{em}). Unless explicitly mentioned, all the photophysical characterization was conducted at room temperature (20 °C). Temperature-dependent measurements were performed with a Peltier-driven temperature-controlled cuvette holder housed in the FLS1000.

1.2. Femtosecond Transient Absorption Spectroscopy (fs-TA)

A fs-TA system was used based on the HELIOS FIRE (Ultrafast Systems), coupled with a femtosecond laser system (Coherent). The details were reported elsewhere.[1] Temperature-controlled experiments were performed with a standalone Peltier-driven temperature-controlled cuvette holder (Flash 300, Quantum Northwest), controlled by T-App software (Quantum Northwest). Datasets obtained were processed and analyzed with the software Surface Xplorer (Ultrafast Systems) via fluorescence background subtractions, applied chirp correction, time-zero adjustments, single value decomposition, global fitting, and kinetic fitting. Global fitting with sequential modeling was performed with ASUfit 3.0.[2] We used global fitting to analyze the data set in the spectral region from ~330 to 700 nm with a sequential, irreversible, kinetic model ($A \rightarrow B \rightarrow C \rightarrow \cdots$). In the data set in DMF, we assumed that back charge recombination (bCR) reactions could be ignored on the assumption that the energy losses are large enough that the reverse reaction rates are not significant. The spectral profiles obtained from analysis with a sequential scheme are called evolution-associated decay spectra (EADS).[3] While this does not necessarily result in spectra representing pure intermediate states, and rather each EADS corresponds in general to a mixture of states, it can provide a simple way of dissecting the progression of spectral changes.[4]

1.3. Electrochemistry

Cyclic voltammetry measurements were conducted on all three samples based on a 600E Electrochemical Analyzer/Workstation (CH Instruments). This system was equipped with a standard three-electrode cell comprised of a pseudo-Ag reference electrode, a Pt wire counter electrode, and a 3 mm glassy carbon-disk working electrode in a *N*,*N*-Dimethylformamide (DMF), acetonitrile (MeCN) or dichloromethane (DCM) solution of 0.1 M tetrabutylammonium hexafluorophosphate ($TBA^+PF_6^-$). Datasets were processed and analyzed with the software CHI600e (CH Instruments). Potentials measured are referenced vs. $Fc^{+/0}$; ferrocene was introduced before measurements were conducted. Spectroelectrochemical measurements of BD and $BDPhMe_4$ were performed with a honeycomb spectroelectrochemical cell (PINE research) coupled to the 600E Electrochemical Analyzer/Workstation. Samples were prepared in MeCN with 0.1 M $TBA^+PF_6^-$.

The comproportionation constant was calculated by the equation

$$K_\mathrm{c} = \exp\left(\frac{F\left(E_\mathrm{red}^\mathrm{n+1} - E_\mathrm{red}^\mathrm{n}\right)}{RT}\right) = \exp\left(\frac{-F\left(\Delta G_\mathrm{c}^\mathrm{n}\right)}{RT}\right) \qquad \text{(S1)}$$

where n is an integer, F is the Faraday constant, R is the molar gas constant, and ΔG_C is expressed in units of electron volts.

1.4. Computations

Computations were carried out with Gaussian16.[5] The geometries were optimized with B3LYP[6, 7] or ωB97XD[8] functional in density functional theory (DFT) calculations. Calculations on radical anions and cations were spin-unrestricted. The 6-31+G(d) or Def2SVP basis set was used for the geometry optimization and TDDFT single-point energy calculations. The Def2SVP basis set was previously used to probe the potential energy surface (PES) of structurally similar BODIPY dimers.[9] The polarizable continuum model (PCM)[10-12] or conductor-like PCM (CPCM)[13, 14] was used as implemented in Gaussian16, unless otherwise noted.

The calculations of PES were performed by restricting the torsion angle between a BODIPY core and a phenyl ring. For the dimers, only one of the torsion angles was scanned, while the other torsion was not fixed and optimized unless otherwise noted.

The transfer integrals were calculated by the energy-splitting in dimer (ESID) model.[15] We took the transfer integral for hole (electron) transfer as half the energetic differences of the HOMO and HOMO-1 (LUMO and LUMO+1) energy levels of a molecular dimer.

1.5. Synthesis

1.5.1. β-coupled BODIPY Dimers

The synthetic scheme of the β-coupled homo dimers is shown in **Scheme S1**.

Scheme S1. Synthetic scheme of aryl bridged β-coupled BODIPY dimers.

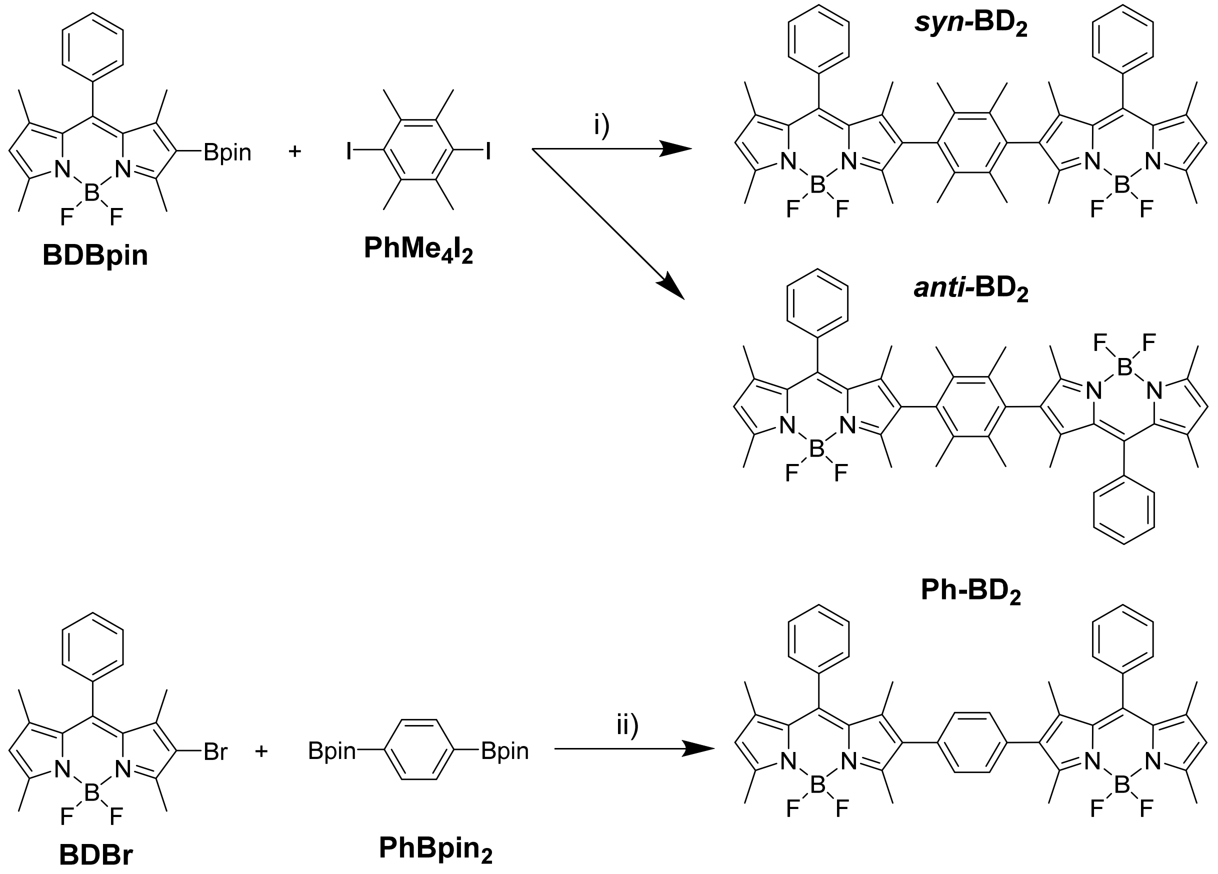

i) PEPPSI^{TM}-IPr/KOH; ii) Pd(OAc)$_2$/SPhos/K$_3$PO$_4$.

We used the PEPPSI^{TM}-IPr precatalyst[16, 17] to perform the Suzuki-Miyaura coupling of diiodotetramethylbenene (PhMe$_4$I$_2$), a structurally hindered (deactivated) substrate, with mono-borylated BODIPY (BDBpin). The BD dimer with an unsubstituted benzene ring was similarly synthesized via Suzuki coupling (with the combination of Pd(OAc)$_2$ and SPhos[18]), using a mono-brominated BD (BDBr) and diboronpinacolatebenzene (PhBpin$_2$). The direct β-β coupled BODIPY dimer without a bridge (BD$_2$) was synthesized in a similar manner described previously.[19] The Suzuki coupling of BDBpin and $PhMe_4I_2$ did not proceed to completion under the same conditions for synthesizing Ph-BD_2 and BD_2.

***syn*- and *anti*-BD_2:** BDBpin (75 mg, 0.17 mmol), $PhMe_4I_2$ (33 mg, 0.087mmol), [1,3-bis(2,6-diisopropylphenyl)imidazol-2-ylidene](3-chloropyridyl)palladium(II) dichloride (PEPPSI™-IPr catalyst, Aldrich, 2.3 mg, 0.0033 mmol), and potassium hydroxide (KOH, 28 mg, 0.50 mmol) were added to a 1-dram reaction vial, degassed, and placed under nitrogen. Anhydrous dioxane (0.65 mL) was added to the reaction vial. The contents of the flask were then heated to 65°C and left for 2.5 hours. The resulting mixture was diluted with 20 mL CH_2Cl_2 and washed three times with equal parts brine. The organic phase was dried over $MgSO_4$, filtered, and evaporated. The crude was then further purified by silica gel column chromatography (CH_2Cl_2/hexanes, 1:3) to afford *anti*-BD_2 as an orange solid (33 mg, 51%). Afterward, the column was increased to 100% CH_2Cl_2 to afford *syn*-BD_2 as a red solid (19 mg, 29%).

***anti*-BD_2:** ^{1}H NMR (300 MHz, $CDCl_3$) δ 7.54 – 7.44 (m, 6H), 7.38 – 7.32 (m, 4H), 5.99 (s, 2H), 2.57 (s, 6H), 2.24 (s, 6H), 1.89 (s, 12H), 1.39 (s, 6H), 1.07 (s, 6H); ^{13}C NMR (75 MHz, $CDCl_3$) δ 154.95, 142.89, 141.63, 140.36, 135.36, 134.15, 133.48, 132.21, 131.66, 131.52, 129.25, 129.06, 128.21, 121.07, 77.58, 76.74, 29.86, 17.71, 14.72, 14.51, 13.21, 12.68.

***syn*-BD_2:** ^{1}H NMR (400 MHz, $CDCl_3$) δ 7.49 – 7.42 (m, 6H), 7.36 – 7.32 (m, 4H), 5.99 (s, 2H), 2.58 (s, 6H), 2.31 (s, 6H), 1.89 (s, 12H), 1.39 (s, 6H), 1.02 (s, 6H); ^{13}C NMR (101 MHz, $CDCl_3$) δ 155.12, 154.99, 142.84, 141.54, 140.20, 135.43, 134.19, 133.49, 132.24, 131.64, 131.53, 129.20, 129.00, 128.26, 121.08, 77.48, 76.84, 29.85, 17.70, 14.72, 14.48, 13.31, 12.57. HRMS (ES+) m/z: [M+H]+ calcd 779.4090, found 779.4103.

Ph-BD$_2$: BDBr (75 mg, 0.18 mmol), PhBpin$_2$ (31 mg, 0.093 mmol), Pd(OAc)$_2$ (2.1 mg, 0.0093 mmol), SPhos (7.6 mg, 0.018 mmol), and potassium phosphate tribasic (K$_3$PO$_4$, 119 mg, 0.56 mmol) were added to a 1-dram reaction vial, degassed, and placed under nitrogen. Toluene (0.70 mL) and water (0.070 mL) were then added to the reaction vial. The contents of the flask were then heated to 80°C and left overnight. The resulting mixture was diluted with 25 mL of CH$_2$Cl$_2$ and washed three times with equal parts brine. The organic phase was dried over MgSO$_4$, filtered, and evaporated. The crude was then further purified by silica gel column chromatography (CH$_2$Cl$_2$/hexanes, 3:1) to afford the pure product as a red solid (32 mg, 48%). ^{1}H NMR (400 MHz, CD$_2$Cl$_2$) δ 7.54 – 7.47 (m, 6H), 7.37 – 7.31 (m, 4H), 7.31 (s, 1H), 7.18 (s, 3H), 6.03 (s, 2H), 2.52 (s, 6H), 2.49 (s, 6H), 1.39 (s, 6H), 1.33 (s, 6H).

BDBpin: BDBr (500 mg, 1.2 mmol), bis(pinacolato)diboron (B$_2$pin$_2$, 380 mg, 1.5 mmol), Pd(OAc)$_2$ (14 mg, 0.062 mmol), tris(4-methoxyphenyl)phosphine (24 mg, 0.068 mmol), and cesium carbonate (Cs$_2$CO$_3$, 610 mg, 1.9 mmol) were added to a 5-dram reaction vial, degassed, and placed under nitrogen. Anhydrous dioxane (5.0 mL) was added to the reaction vial. The contents of the flask were then heated to 80°C and left overnight. The resulting mixture was diluted with 40 mL of CH$_2$Cl$_2$ and washed three times with equal parts brine. The organic phase was dried over MgSO$_4$, filtered, and evaporated. The crude was then further purified by silica gel column chromatography (CH$_2$Cl$_2$/hexanes, 1:1) to afford the pure product as an orange solid powder (520 mg, 92%). ^{1}H NMR (300 MHz, CDCl$_3$) δ 7.51 – 7.44 (m, 3H), 7.28 – 7.23 (m, 2H), 6.00 (s, 1H), 2.75 (s, 3H), 2.56 (s, 3H), 1.59 (s, 3H), 1.36 (s, 3H), 1.26 (s, 12H), ^{13}C NMR (101 MHz, CDCl$_3$) δ 163.32, 155.88, 152.47, 143.67, 142.14, 135.38, 132.44, 131.96, 131.02, 129.27, 129.03, 128.12, 121.82, 82.92, 77.48, 76.84, 29.85, 24.97, 14.99, 14.77, 14.57, 14.49. HRMS (ES+) m/z: [M+H]+ calcd 451.2543, found 451.2543.

PhMe$_4$Bpin: PhMe$_4$Br (500 mg, 2.3 mmol), B$_2$pin$_2$ (720 mg, 2.8 mmol), Pd(OAc)$_2$ (26 mg, 0.12 mmol), tris(4-methoxyphenyl)phosphine (46 mg, 0.13 mmol), and Cs$_2$CO$_3$ (1.1 g, 3.5 mmol) were added to a 5-dram reaction vial, degassed, and placed under nitrogen. Anhydrous dioxane (7.8 mL) was added to the reaction vial. The contents of the flask were then heated to 80°C and left overnight. The resulting mixture was diluted with 50 mL of CH$_2$Cl$_2$ and washed three times with equal parts brine. The organic phase was dried over MgSO$_4$, filtered, and evaporated. The crude was then further purified by silica gel column chromatography (CH$_2$Cl$_2$/hexanes, 1:2) to afford the pure product as an oily, yellow liquid (340 mg, 56%). ^{1}H NMR (400 MHz, CDCl$_3$) δ 6.97 (s, 1H), 2.34 (s, 6H), 2.25 (s, 6H), 1.47 (s, 12H).

BDPhMe$_4$: BDBr (50 mg, 0.12 mmol), PhMe$_4$Bpin (39 mg, 0.15 mmol), Pd(OAc)$_2$ (1.4 mg, 0.0062 mmol), SPhos (5.1 mg, 0.012 mmol), and K$_3$PO$_4$ (79 mg, 0.37 mmol) were added to a 1-dram reaction vial, degassed, and placed under nitrogen. Toluene (0.45 mL) and water (0.045 mL) were then added to the reaction vial. The contents of the flask were then heated to 80°C and left overnight. The resulting mixture was diluted with 20 mL of CH$_2$Cl$_2$ and washed three times with equal parts brine. The organic phase was dried MgSO$_4$, filtered, and evaporated. The crude was then further purified by silica gel column chromatography (CH$_2$Cl$_2$/hexanes, 1:5) to afford the pure product as an orange solid (17 mg, 57%). ^{1}H NMR (300 MHz, CDCl$_3$) δ 7.53 – 7.44 (m, 3H), 7.38 – 7.31 (m, 2H), 6.95 (s, 1H), 5.99 (s, 1H), 2.58 (s, 3H), 2.27 (s, 3H), 2.22 (s, 6H), 1.87 (s, 6H), 1.39 (s, 3H), 1.06 (s, 3H); ^{13}C NMR (75 MHz, CDCl$_3$) δ 155.14, 154.85, 142.81, 141.56, 140.32, 135.37, 133.86, 133.64, 133.56, 132.57, 131.62, 131.48, 131.09, 129.24, 129.05, 128.21, 121.04, 77.58, 76.74, 29.85, 20.36, 16.81, 14.71, 14.48, 13.20, 12.52. HRMS (ES+) m/z: [M+H]+ calcd 457.2626, found 457.2619.

PhBpin: PhBr (2.0 g, 1.4 mL, 13 mmol), B_2pin_2 (6.47 g, 25 mmol), [1,1-bis(diphenylphosphino)ferrocene]dichloropalladium(II) (Pd(dppf)Cl_2, 670 mg, 0.92 mmol), and potassium acetate (KOAc, 3.8 g, 38 mmol) were added to a 100 mL reaction flask, degassed, and placed under nitrogen. *N*, *N*-Dimethylformamide (DMF, 51 mL) was added to the reaction flask. The contents of the flask were then heated to 80°C and left overnight. The resulting mixture was diluted with 50 mL of CH_2Cl_2 and washed three times with equal parts brine. The organic phase was dried over $MgSO_4$, filtered, and evaporated. The crude was then purified by silica gel column chromatography (CH_2Cl_2/hexanes, 1:3) to afford the pure product as an oily, yellow liquid (1.95 g, 75%).

BDPh: BDBr (150 mg, 0.37 mmol), PhBpin (91 mg, 0.45 mmol), $Pd(OAc)_2$ (4.2 mg, .019 mmol), SPhos (15 mg, 0.037 mmol), and K_3PO_4 (296 mg, 1.4 mmol) were added to a 1-dram reaction vial, degassed, and placed under nitrogen. Toluene (1.3 mL) and water (0.13 mL) were then added to the reaction vial. The contents of the flask were then heated to 80°C and left overnight. The resulting mixture was diluted with 20 mL of CH_2Cl_2 and washed three times with equal parts brine. The organic phase was dried $MgSO_4$, filtered, and evaporated. The crude was then further purified by silica gel column chromatography (CH_2Cl_2/hexanes, 1:5) to afford the pure product as an orange solid (136 mg, 91%). ^{1}H NMR (400 MHz, $CDCl_3$) δ 7.52 – 7.46 (m, 3H), 7.40 – 7.35 (m, 2H), 7.34 – 7.31 (m, 2H), 7.30 – 7.26 (m, 1H), 7.16 – 7.12 (m, 2H), 6.01 (s, 1H), 2.59 (s, 3H), 2.52 (s, 3H), 1.39 (s, 3H), 1.30 (s, 3H); ^{13}C NMR (101 MHz, $CDCl_3$) δ 155.77, 154.18, 143.38, 142.09, 139.32, 135.37, 133.87, 131.88, 131.17, 130.31, 129.32, 129.13, 128.43, 128.16, 127.17, 121.49, 77.48, 76.84, 14.77, 14.55, 13.48, 12.79. HRMS (ES+) m/z: [M+H]+ calcd 401.2000, found 401.1977.

1.5.2. *meso*-coupled BODIPY Dimers

We synthesized the orthogonally linked BODIPY dimer with tetramethylbenzene as a bridge ($m_{12}Ph$) from 1,4-dialdehyde-2,3,5,6-tetramethylbenzene (Scheme S2). 1,4-dialdehyde-2,3,5,6-tetramethylbenzene was synthesized as described before.[20] We synthesized the unsubstituted benzene analogue (m_8Ph) in a similar manner as described before. The synthesis and characterizations of m_8Ph,[9] BDBr,[21] and a monomer $BDMe_2$[22] were previously reported.

Scheme S2. Synthetic scheme of $m_{12}Ph$.

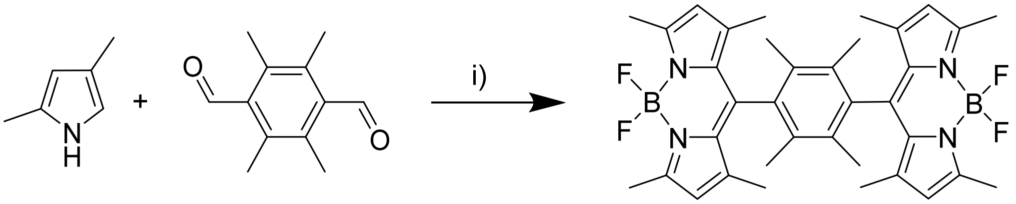

i) TFA, DDQ, DIPEA, BF_3OEt_2

$m_{12}Ph$: 1,4-Dialdehyde-2,3,5,6-tetramethylbenzene (230 mg, 1.2 mmol) and 2,4-dimethylpyrrole (575 mg, 0.63 mL, 6.0 mmol) were dissolved in 5 mL of CH_2Cl_2 under a nitrogen atmosphere. A drop of trifluoroacetic acid (TFA) was added, and the reaction was stirred for 3 hours. The reaction was monitored with TLC to ensure the total consumption of the aldehyde. 2,3-dichloro-4,5-dicyanobenzoquinone (DDQ, 549 mg, 2.4 mmol) was then added to the reaction and was stirred for 1 hour. The reaction mixture was then degassed with nitrogen, after which *N*,*N*-diisopropylethylamine (DIPEA, 2 mL, 22 mmol), and boron trifluoride ethyl etherate ($BF_3.OEt_2$, 2.5 mL, 20 mmol) were added, and the reaction was stirred for 1 hour. Then, the reaction mixture was washed with brine, dried over MgSO4, filtered, and evaporated in vacuo. The crude was then further purified by silica gel column chromatography (CH_2Cl_2/hexanes, 1:1) to afford the pure product as an orange powder (9 mg, 1.2%). ^{1}H NMR (400 MHz, $CDCl_3$) δ 5.98 (s, 4H), 2.58 (s, 12H), 2.16 (s, 12H), 1.46 (s, 12H). HRMS (ES+) m/z: [M+H]+ calcd 627.3448, found 627.3477.

2. MJL Equation and Fitting

2.1. The MJL equation is expressed as the following

$$k_{\mathrm{ET}} = \frac{2\pi}{\hbar}|V_{\mathrm{if}}|^2 \frac{1}{\sqrt{4\pi\lambda_{\mathrm{S}}k_{\mathrm{B}}T}} \sum_{w=0}^{\infty}(e^{-S}\frac{S^w}{w!})\exp\left[-\frac{(\lambda_{\mathrm{S}}+\Delta G^0+w\hbar\omega)^2}{4\lambda_{\mathrm{S}}k_{\mathrm{B}}T}\right] \quad \text{(S1)}$$

where V_{if} is the electronic coupling, $S = \frac{\lambda_{\mathrm{V}}}{\hbar\omega}$ is the Huang-Rhys factor characterizing the strength of e-v coupling, and ω is only one high frequency of the coupled quantum mechanical vibration modes. This study sets the vibrational quantum $\hbar\omega$ as 1500 cm^{-1} (0.186 eV) based on aromatic C=C stretching vibrations.[23] The internal reorganization energy λ_{V} was assumed to be temperature-independent and fixed to 0.22 eV based on the DFT calculation. Following procedure,[24] we used the SMD solvation model[25] to calculate the internal reorganization energy. Note that while the absolute values of V_{if} and λ_{S} obtained by fittings described below depend on the values of $\hbar\omega$ and λ_{V} of our choice, the observed trends still hold.

2.2. We fitted the temperature-dependent charge recombination constants of $\mathrm{m_{12}Ph}$ in DMF with the rest of the parameters (V_{if}, ΔG^0_{CR}, and λ_{S}) being variables. We assumed V_{if} is temperature-independent (please see the main text and **Supplementary Information** Section 4 for details) while ΔG^0 and λ_{S} are temperature-dependent. ΔG^0_{CR} and λ_{V} are expressed in the forms of

$$\Delta G^0_{\mathrm{CR}} = a + bT \quad \text{(S2)}$$

$$\lambda_{\mathrm{S}} = c + dT \quad \text{(S3)}$$

The constants b and d are $\frac{\partial \Delta G^0_{\mathrm{CR}}}{\partial T}$ and $\frac{\partial \lambda_{\mathrm{S}}}{\partial T}$, respectively.[26] For ΔG^0_{CR}, we constrained the parameters (a and b) to give the experimentally estimated $\Delta G^0_{\mathrm{CR}} \sim -2.21$ eV at $T = 20$ °C (**Table 2** of the main text). The best fit of the data to eq. S1 is shown in **Figure A1** with the parameters $V_{\mathrm{if}} = 0.0031$ eV (or 25 cm^{-1}), a = -2.17, b = -1.3e-4, c = 0.93, d = -8.5e-4 (best fit in the figure). The fit provides the total reorganization energy ($\lambda = \lambda_V + \lambda_S = 0.91$ eV) at $T = 20$ °C, which is reasonably close to λ obtained for charge separation ($\lambda = 0.8$ eV, **Table S4**). The fit also showed that both ΔG^0_{CR} and λ_S decrease with increasing temperature (b and d are negative).

We could fit the data equally well when we assumed ΔG^0_{CR} is temperature independent ($\Delta G^0_{\mathrm{CR}} = -2.21$ eV across the temperature range). The "fit with ΔG fixed" in **Figure A1** gave a slightly higher $V_{\mathrm{if}} = 0.0043$ eV (or 34 cm^{-1}). However, we could not fit the data to eq. S1 when we assumed λ_S is temperature independent ($\lambda_S = 0.69$ eV). We showed the curve as "λ_S fixed" in **Figure A1**.

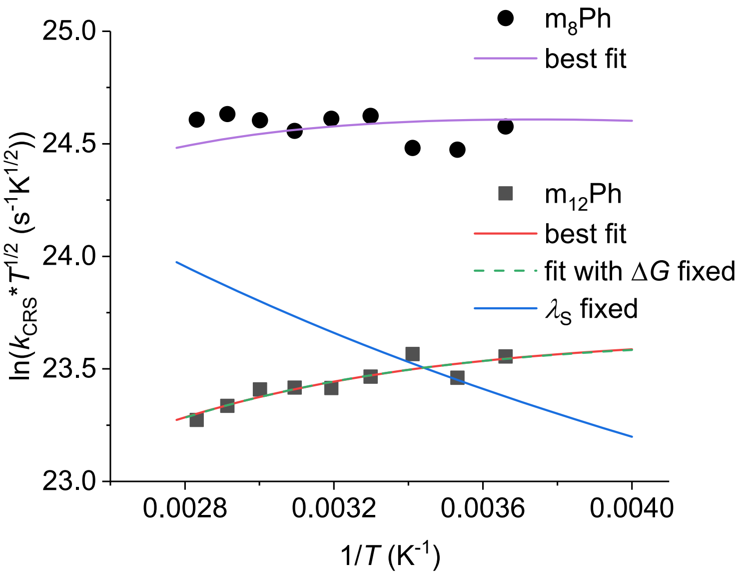

Figure A1. Fitting temperature-dependent charge recombination rates of m$_{12}$Ph in DMF to the MJL equation (eq. S1).

2.3. Using the parameters (a, b, c, d of eq. S2 and S3) of the best fit from m$_{12}$Ph, we fitted the temperature-dependent charge recombination constants of m$_8$Ph to eq. S1. Here, the coupling is assumed to be temperature-dependent in the form of a sigmoidal function: $V_{\mathrm{if}} = \frac{\alpha}{1+\exp(-\beta T)}$. We have V_{if} ($T = 0$ K) = $V_0 = \alpha/2$ in this form. We used a sigmoidal function as a model function because it can capture the two limiting cases: the lowest coupling at lower temperatures where the torsion angle is "fixed" at the optimal angle of φ ~90° and the highest coupling at higher temperatures where the torsion angle can deviate most from φ ~90°. The best fit gave $V_0 = 0.0144$ eV (or 116 cm^{-1}) and $\beta = 0.0041\ T^{-1}$. Based on these parameters, we have V_{if} (T = 20 °C) = 0.0055 eV (or 44 cm^{-1}) for m_8Ph. The fit satisfactorily gave a higher coupling for m_8Ph than for $m_{12}Ph$. We want to emphasize that the obtained coupling constants (and the used sigmoidal form) are estimates, yet these fittings clearly illustrate that temperature-dependent V_{if} can modify how k_{CR} depends on temperature and our experimental observations.

3. Electrochemical Characterizations

Electrochemical measurements were performed on the molecules investigated. The data of the cyclic voltammetry measurements are summarized in **Table 3** of the main text and **Table S1**. The voltammograms showed one reduction potential of the radical cation that is almost the same among all the molecules: E_{red} (●+/0) ~ 0.7 V vs. $\mathrm{Fc}^{+/0}$. *syn*- and *anti*-BD_2 exhibit the reduction potential of the neutral at E_{red}^{2} (0/●-) ~ -1.56 V, the same as the monomers (BDPhMe_4 and BD). These values agree with those measured in MeCN and those previously recorded for the structurally similar BODIPYs.[27-29] On the other hand, the reductive peak of BD_2 is now split into two one-electron steps: E_{red}^{2} and E_{red}^{3}(●-/2-). The reductive process is resolved with the peaks being split by ~0.18 V with the comproportionation constant, K_{C} ~ 890 (**Figure S2**), indicating a slight delocalization of the first added electron over the two BODIPY units. Such splitting was observed previously only for closely spaced co-facial BD dimers with splittings of 0.15 and 0.17 V with a distance between monomers of ~ 5.50 and 4.7 Å, respectively.[30] A splitting on the reduction potential of radical cations was also observed for a closely spaced co-facial porphyrin dimer; the splitting was ~0.20 V for the dimer with a distance between monomers of ~ 3.8 Å.[31] The lack of splitting in the other dimers studied here indicates that the addition of the first and second electrons are energetically similar for them; $E_{red}^{2} \sim E_{red}^{3}$ with negligible K_{C}.

We also observed the peaks that correspond to the third addition of electrons (E_{red}^{4}) at around the same potential among the series (~ -2.4 – 2.5 V vs. $\mathrm{Fc}^{+/0}$), except for *anti*-BD_2, which showed a significantly more negative peak. While the data is reproducible, we refrain from commenting further on this more negative peak for *anti*-BD_2 because of its poor solubility in DMF. We could not observe the peaks corresponding to E_{red}^{4} in any of these molecules in DCM, likely because of the narrower electrochemical window.[32] Similarly, the poor solubility of Ph-BD_2 prevented us from making reasonable CV measurements on Ph-BD_2 in DMF. We, therefore, performed CV measurements in DCM (**Table S1**). The E_{red} values for Ph-BD_2 reported in **Table 3** of the main text are estimations using BDPh values in DMF and DCM as a reference. While the reductions of the radical cation (i.e., oxidation) appear irreversible for all BODIPYs in DMF, they are reversible in MeCN and DCM (**Table S1**). In DCM, we observed that the oxidative peaks of *syn*/*anti*-BD_2 and Ph-BD_2 are split into two one-electron steps; the splittings are small ~0.03 and 0.06 V with K_C ~ 3 and 13, respectively. The reduction of the radical cation of BD_2 does not show splitting, instead becoming more negative by ~0.05 V than the corresponding monomers. This observation suggests that a positive charge is partially delocalized over the two units of BD_2 in a less polar solvent DCM.[33] We did not observe a clear peak corresponding to the second electron removal (i.e., second oxidation) for BD_2 within the electrochemical window of 0.1 M $TBA^+PF_6^-$ in DCM. Contrarily, the reduction potential of the neutral BD_2 is now split into two by ~0.14 V with K_C ~ 260. This observation of the splitting in DCM may be due to the effect of ion pairing[34] that becomes stronger in a nonpolar environment.[35, 36]

4. Discussions on the PES

We attribute the differences in the effect of tetramethylbenzene on the photophysics between the β- and *meso*-coupled BODIPY dimers to the change of conformational restrictions by tetramethylbenzene. We determined PES along the phenyl ring's torsion angle (φ) in the β and meso-position. Please note that we could not identify the charge-transfer (or RP) state for the β-coupled dimers in the correct energetic order (below the local/dimer exciton states) by time-dependent DFT calculations with the tested combinations of functionals and solvation models. Nevertheless, the torsional motion between the BODIPY core and the phenyl ring in the direction of electron transfer is the most flexible and deemed essential for the electron transfer process. DFT calculations of the control BODIPY molecules showed that the energy minima and the overall shapes along the torsion angle (φ) remain the same for the local BODIPY singlet excited state, charged states, and the ground states while the energy barriers become somewhat shallower at the charged and excited states (**Figure S9**). Therefore, the following semi-quantitative arguments, using the PES of the ground states, are generally expected to hold. Further computational analysis would provide a more quantitative picture.

The ground state PES as a function of the torsion angle of Ph-BD$_2$ and *syn*-BD$_2$ is reported in **Figure 8b** of the main text. The PES for Ph-BD$_2$ (and the corresponding monomer BDPh) has an energy minimum at φ ~50° (ωB97XD/Def2SVP): two minima in the span of 180° rotation. We can classify Ph-BD$_2$ as a "weak" torsional hindrance case.[37] For the dimers' PES shown in **Figure 8b** of the main text, we scanned only one of the torsion angles, and the other one was optimized, which is φ ~50° for Ph-BD$_2$, regardless of the angle scanned. The tetramethylbenzene bridge fixes the phenylene ring to be more orthogonal to the BODIPY planes (φ ~70° for *syn*-BD$_2$ vs. ~ 50° for Ph-BD$_2$) and lowers the energy barrier for the orthogonal configuration (φ ~ 90°) significantly; ΔE

= E (φ = 90°) - E (optimal φ) = 15 meV vs 37 meV for *syn*-BD$_2$ and Ph-BD$_2$. The actual PES surface along the torsion angle between the BODIPY plane and tetramethylbenzene at the β position somewhat depends upon functionals. For example, it has the lowest energy conformation at φ = 90° when calculated with B3LYP (**Figure A2**).

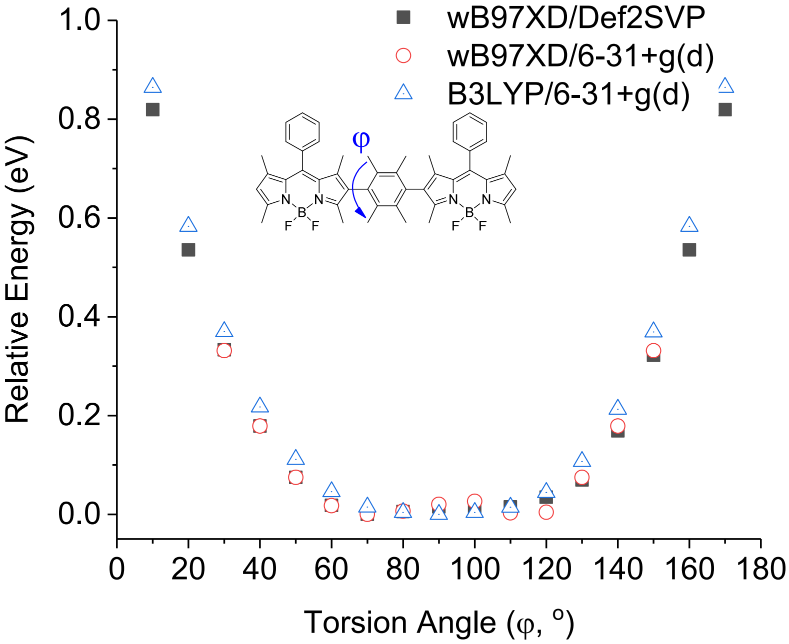

Figure A2. Potential energy surface along the torsion angle (φ) of *syn*-BD$_2$ at B3LYP/6-31+g(d)/CPCM(DMF), wB97XD/6-31+g(d)/CPCM(DMF), and wB97XD/Def2SVP/CPCM(DMF).

Regardless of the actual values, we observed a clear shift of torsion angle at the energy minimum to a more orthogonal configuration from Ph-BD$_2$ to *syn*-BD$_2$. This shift effectively serves as a block to reduce electronic couplings between the two BODIPYs. The electronic couplings between the two BODIPYs are dictated mainly by the torsion angle between the BD core and the phenyl ring, not by the angle between the two BODIPYs, which we can explain by the nearest neighbor perturbation theory model of McConnel for donor-acceptor coupling mediated by a bridge.[38] Accordingly, the electronic coupling, judged by the transfer integrals (or "hopping integrals") of electron and hole (t_E and t_H) in the dimer cases, is smallest when $\varphi \sim 90^o$, slowing down both SBCS and CR, as we observed (**Figure 7b** of the main text).

In contrast, the torsion angle minimum between the BD core and phenyl ring in the *meso*-position is $\varphi = 90^o$. Similarly to the β-position case, the PES minima remain the same for the BODIPY's singlet excited, charged, and ground states (**Figure S9**). Unlike the β-coupled case, the introduction of tetramethylbenzene in the *meso*-position does not alter the optimal φ from m_8Ph to $m_{12}Ph$, while it further restricts the motion with extra methyl groups locking the torsion angle more to the orthogonal configuration for $m_{12}Ph$. This locking raises the energy barrier to access "flatter" conformations of higher electronic couplings, slowing down SBCS and CR (**Figure 7b** of the main text). Please see **Figure 8b** of the main text for the PES for the dimers and **Figure S12** for the control BODIPYs. In addition, we performed a full PES scan along the two torsion angles for m_8Ph, which confirms significant energy barriers for the complete flatter conformations ($\Delta E >> 0.2$ eV, **Figure A3**).

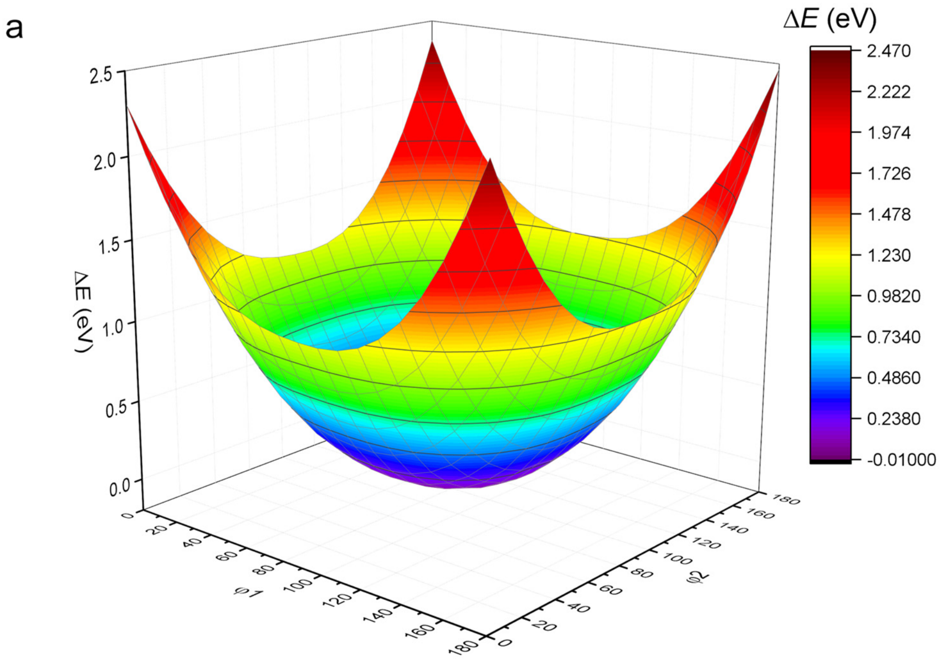

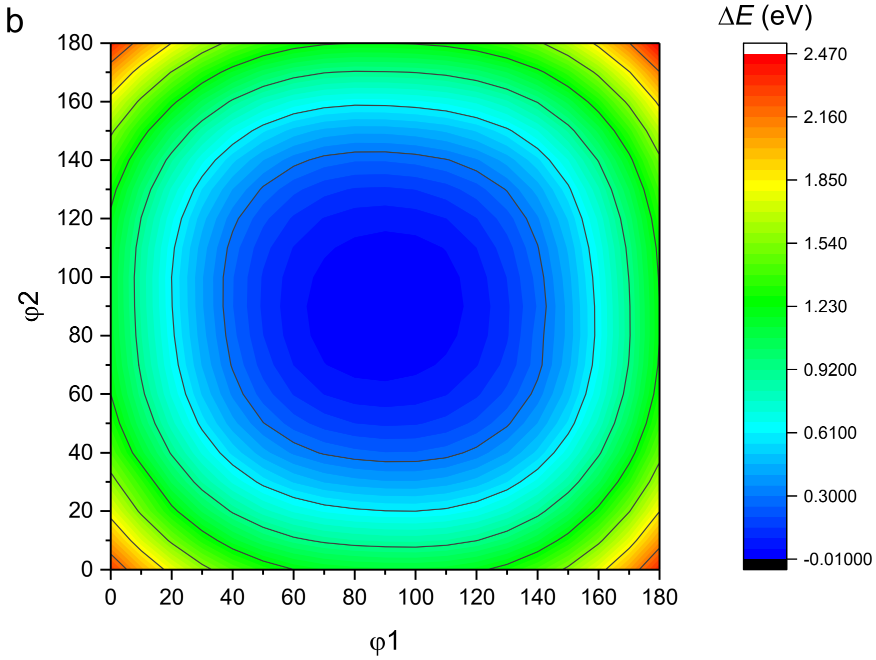

Figure A3. (a) 3D data plot of the PES along the two torsion angles ($\varphi1$ and $\varphi2$) of m8Ph computed at wB97XD/Def2SVP/CPCM(DMF). Δ*E* is defined as the energy difference with respect to the lowest energy on the surface ($\varphi1 = \varphi2 = 90^o$). (b) The contour plot of the 3D plot.

5. Supplementary Figures

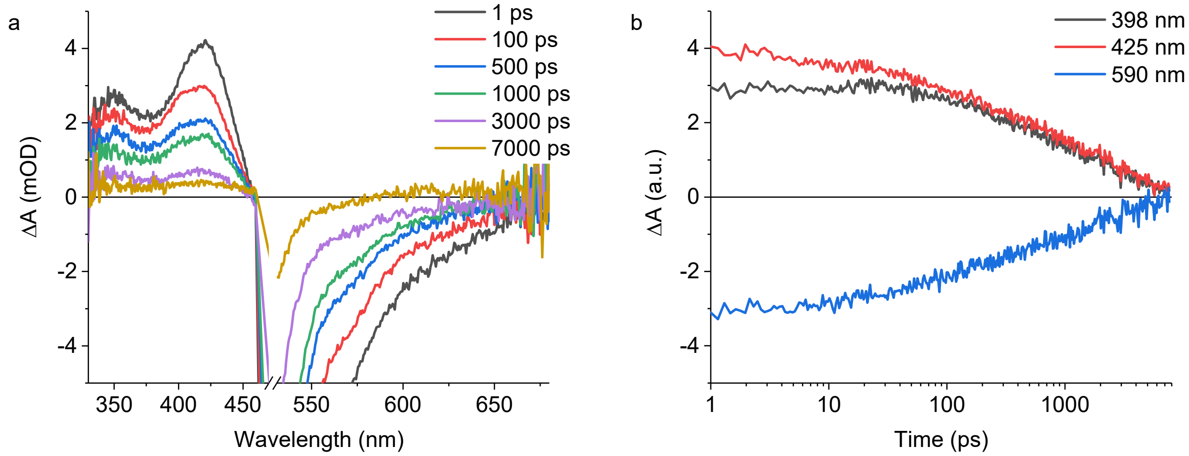

Figure S1. (a) Transient absorption spectra of *syn*-BD$_2$ in chloroform at respective time upon photoexcitation at λ_{ex} = 500 nm. (b) Kinetics traces at 398, 425, and 590 nm.

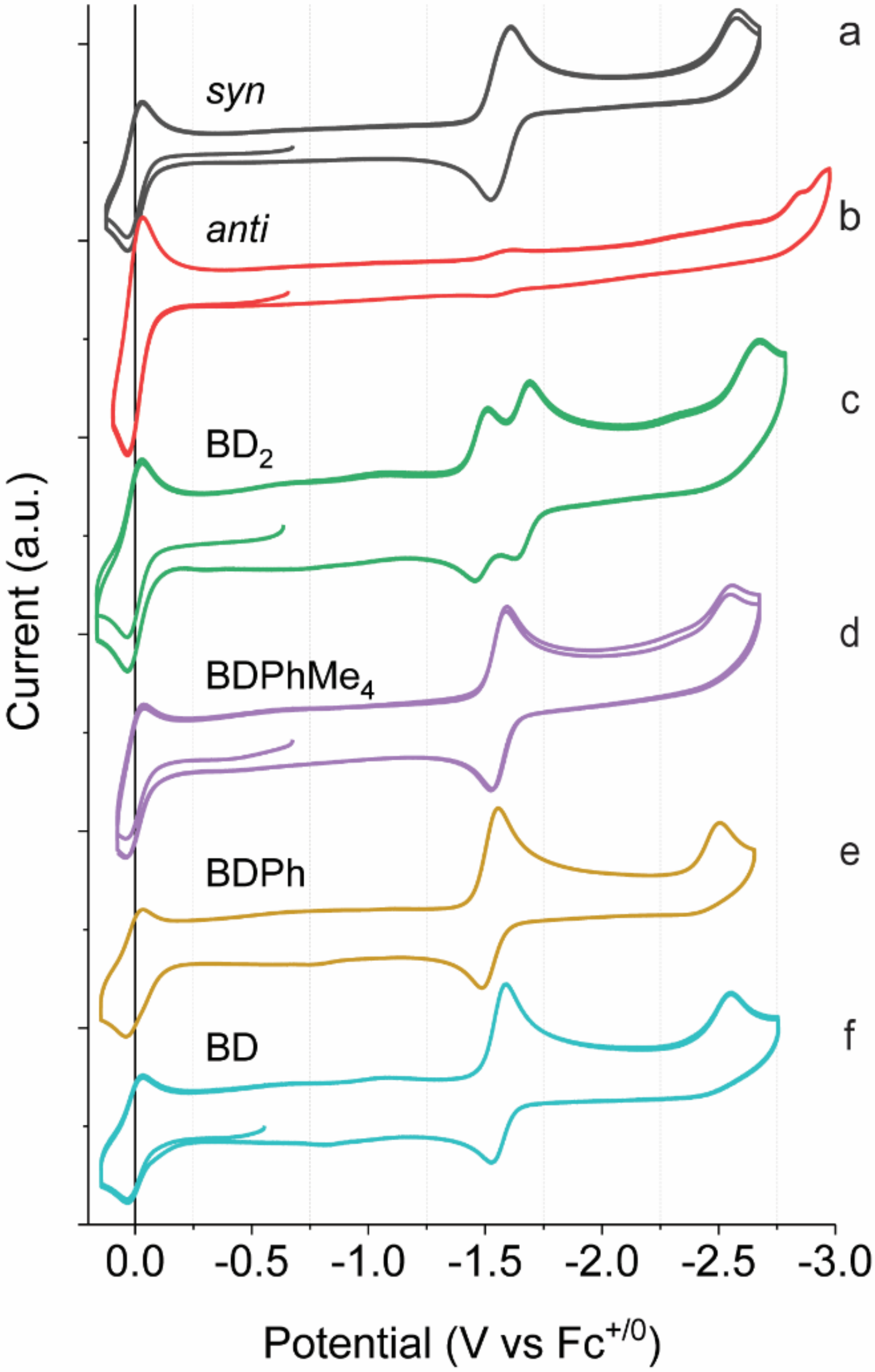

Figure S2. Cyclic voltammograms of the compounds in DMF with 100 mM TBA$^+$PF$_6^-$. Currents are arbitrary. Scan rate = 100 mV s^{-1}. The solid black line indicates 0 V vs Fc$^{+/0}$. Reduction potentials are reported in **Table 3** of the main text. The peaks in this figure correspond to E^2_{red}, E^3_{red}, and E^4_{red}. Please note that we could not perform the measurements of Ph-BD$_2$ in DMF, and therefore the data was not included.

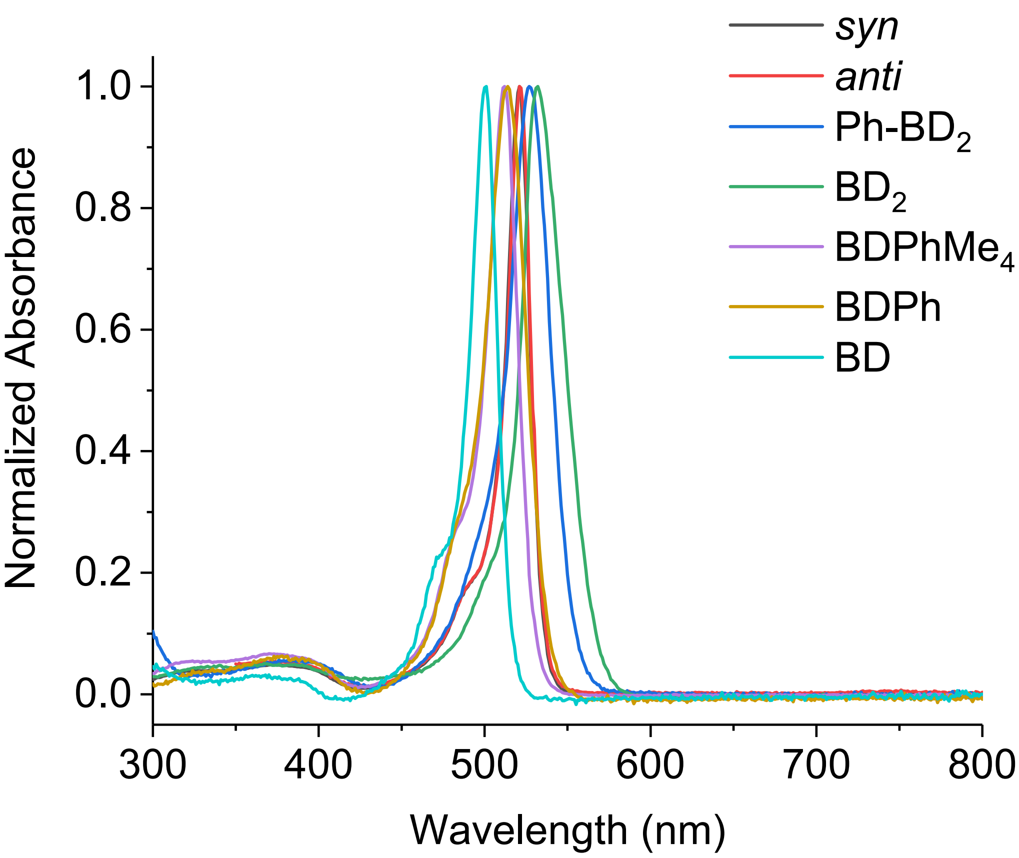

Figure S3. Absorption spectra of the β-coupled BODIPY dimers and monomers in DMF.

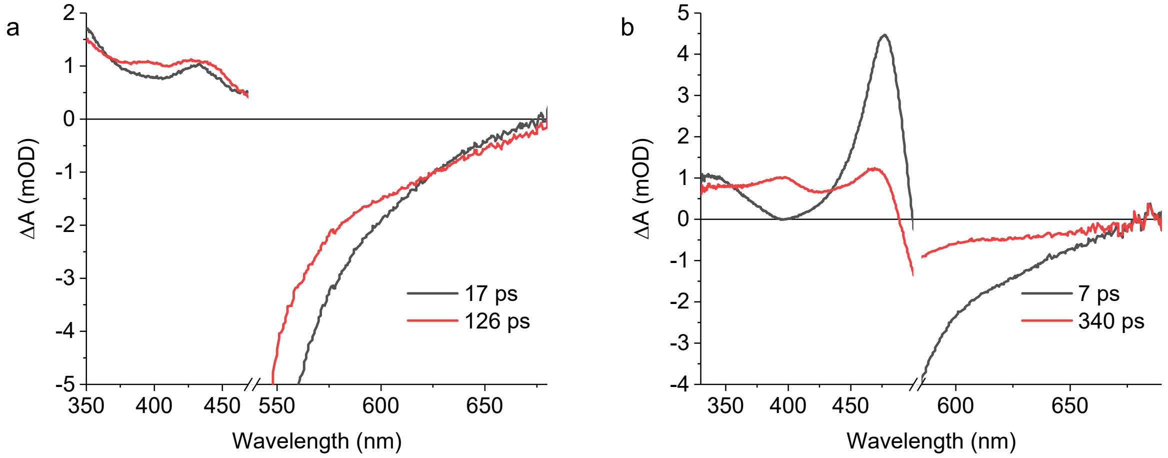

Figure S4. EADS of the fsTA spectra of (a) Ph-BD$_2$ (λ_{ex} = 520 nm) and (b) BD$_2$ (λ_{ex} = 520 nm) in DMF with corresponding lifetimes upon photoexcitation at respective wavelengths.

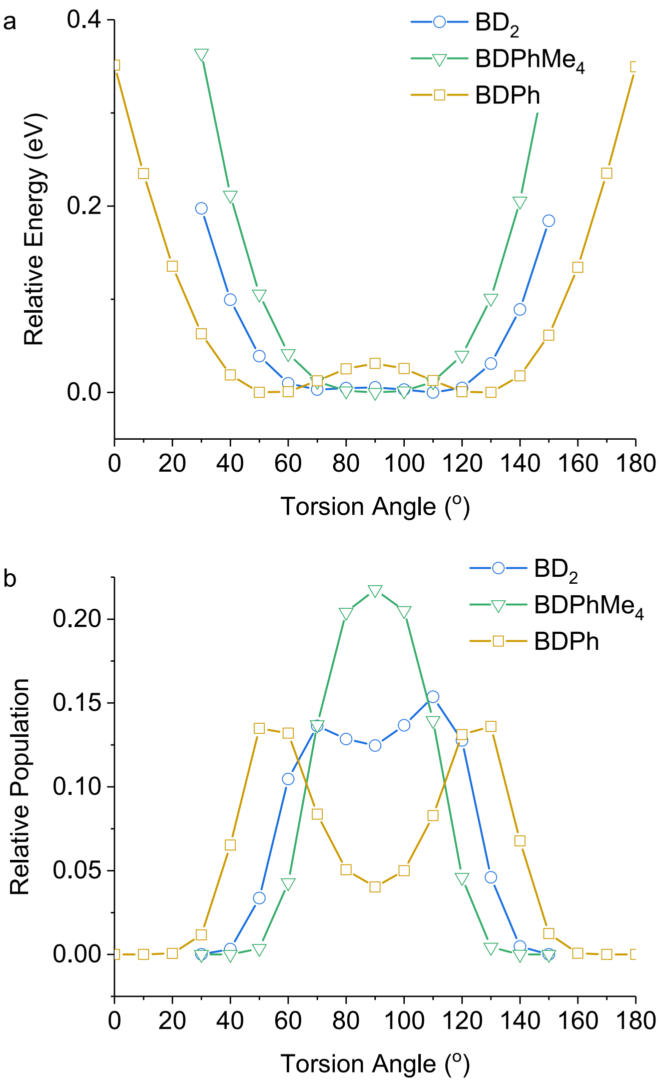

Figure S5. (a) Potential energy surfaces of the ground states of BD_2, $BDPhMe_4$, and BDPh along torsion angle. The calculations were performed at B3LYP/6-31+g(d)/PCM(chloroform). The torsion angle is the angle between two BODIPY for BD2 and the angle between the BODIPY core and a phenyl ring in the β-position for $BDPhMe_4$ and BDPh. (b) Relative population vs. the torsion angle. Relative population was estimated by the Boltzmann distribution for 20 °C**.**

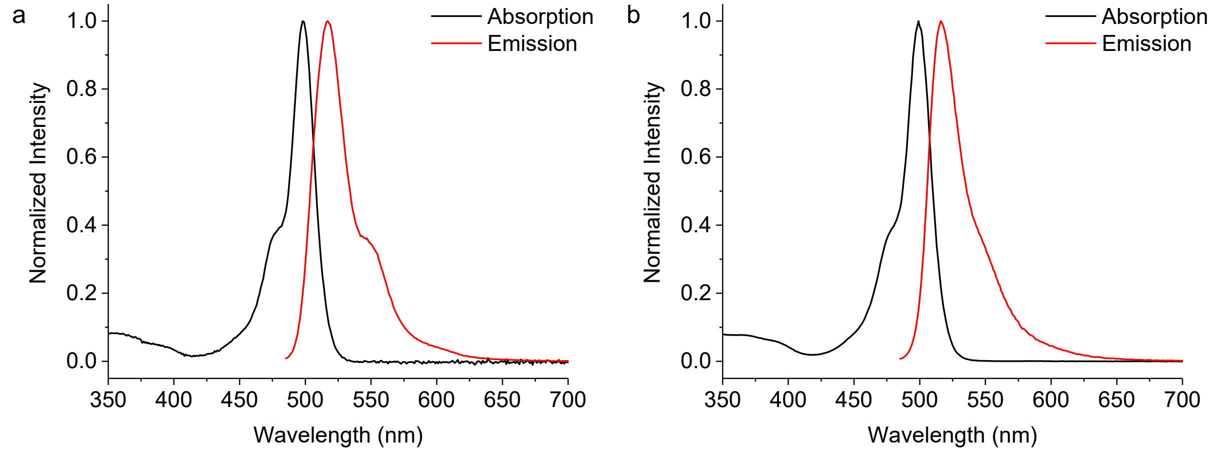

Figure S6. Normalized absorption and emission spectra of (a) $m_{12}Ph$ and (b) m_8Ph in DMF. Emission spectra are taken upon photoexcitation at λ_{ex} = 470 nm.

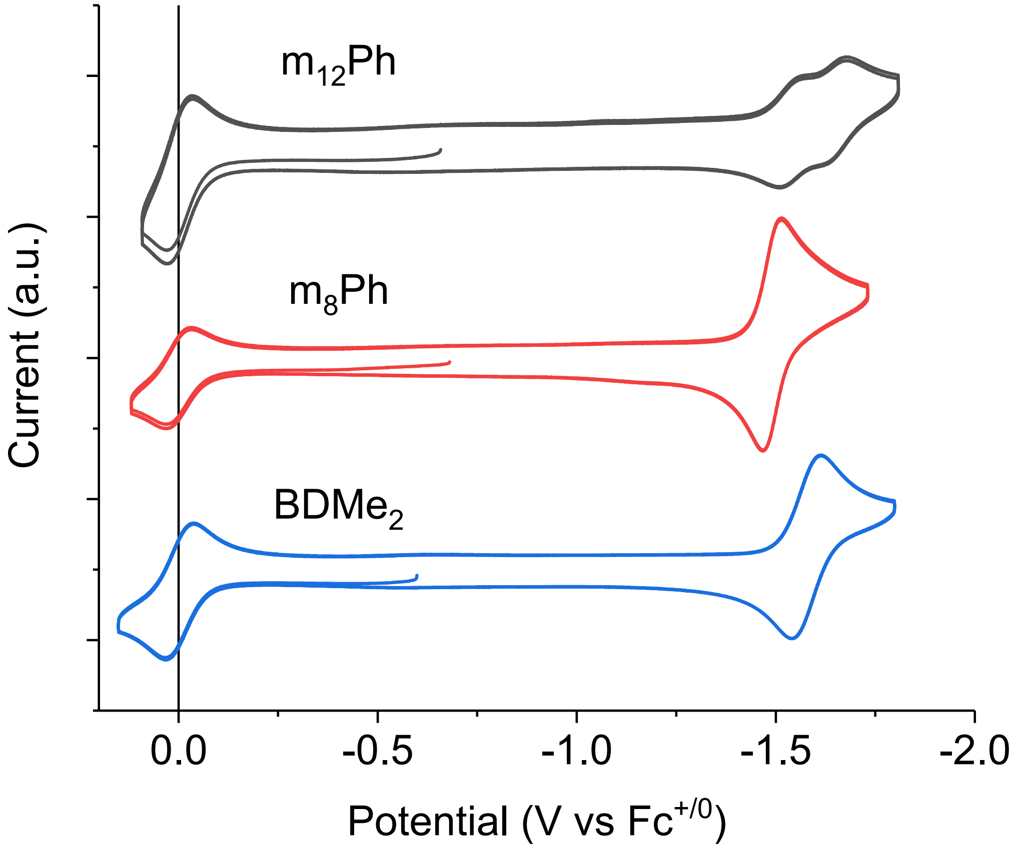

Figure S7. Cyclic voltammograms of the compounds in DMF with 100 mM TBA$^+$PF$_6^-$. Currents are arbitrary. Scan rate = 100 mV s^{-1}. The solid black line indicates 0 V vs. Fc$^{+/0}$. Reduction potentials are reported in **Table 3** of the main text.

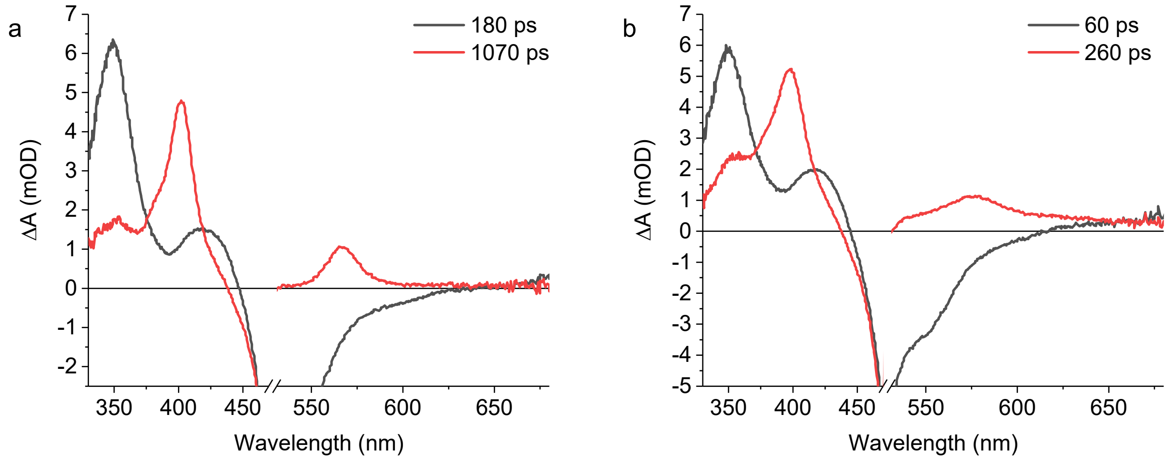

Figure S8. EADS of the fsTA spectra of (a) $m_{12}Ph$ and (b) m_8Ph in DMF with corresponding lifetimes upon photoexcitation at λ_{ex} = 500 nm. The peaks ~400 nm and ~570 nm correspond to the radical cation and anion of BODIPY.

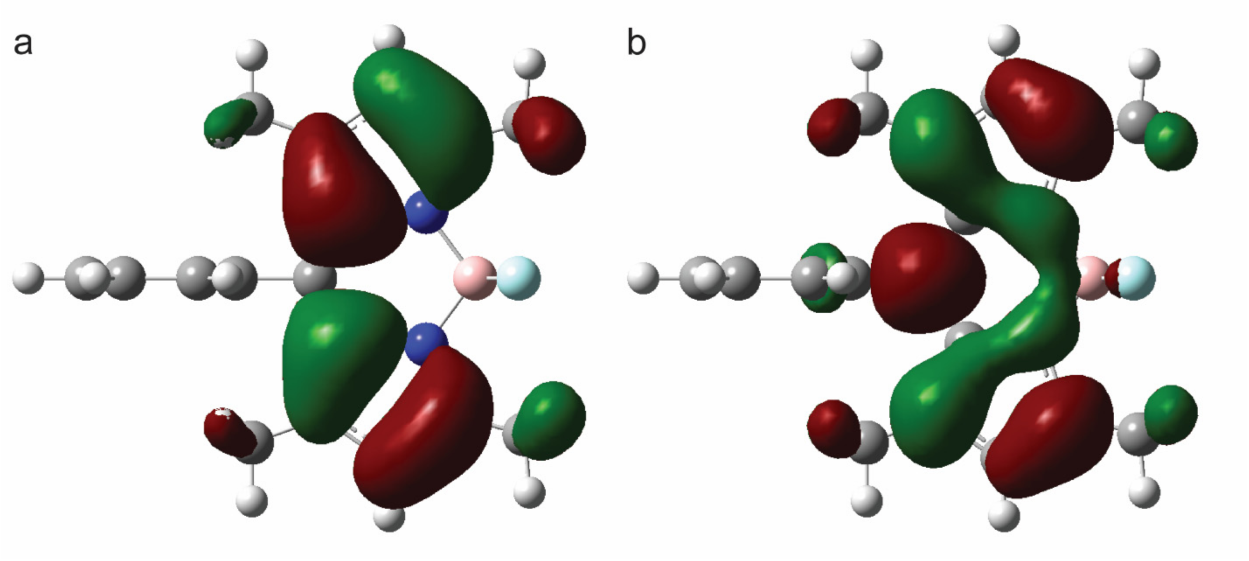

Figure S9. Molecular orbital surfaces of HOMO and LUMO of BD computed at wB97XD/Def2SVP/CPCM(DMF).

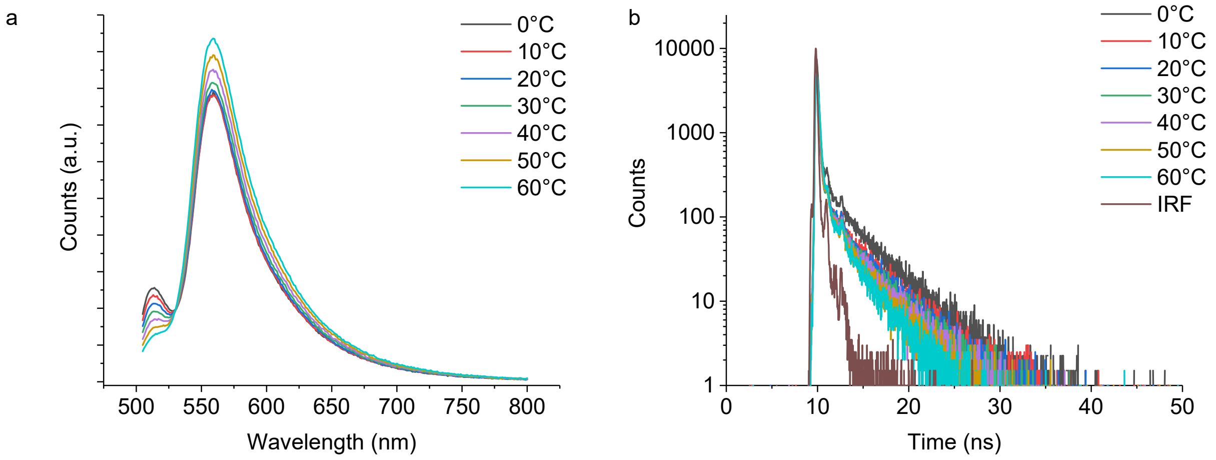

Figure S10. Temperature dependence of fluorescence for Ph-BD$_2$ in DMF from 0 to 60 ºC. (a) Steady-state spectra upon photoexcitation at λ_{ex} = 490 nm. (b) Lifetime measured at λ_{em} = 560 nm upon photoexcitation at λ_{ex} = 506 nm. IRF = instrument response function.

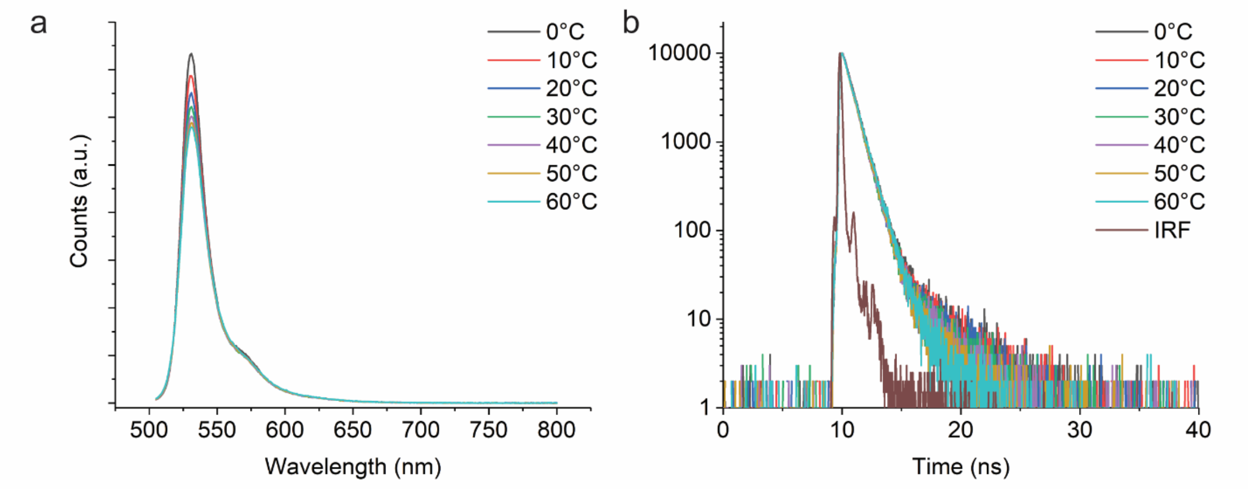

Figure S11. Temperature dependence of fluorescence for *syn*-BD$_2$ in DMF from 0 to 60 ºC. (a) Steady-state spectra upon photoexcitation at λ_{ex} = 490 nm. (b) Lifetime measured at λ_{em} = 560 nm upon photoexcitation at λ_{ex} = 506 nm. IRF = instrument response function.

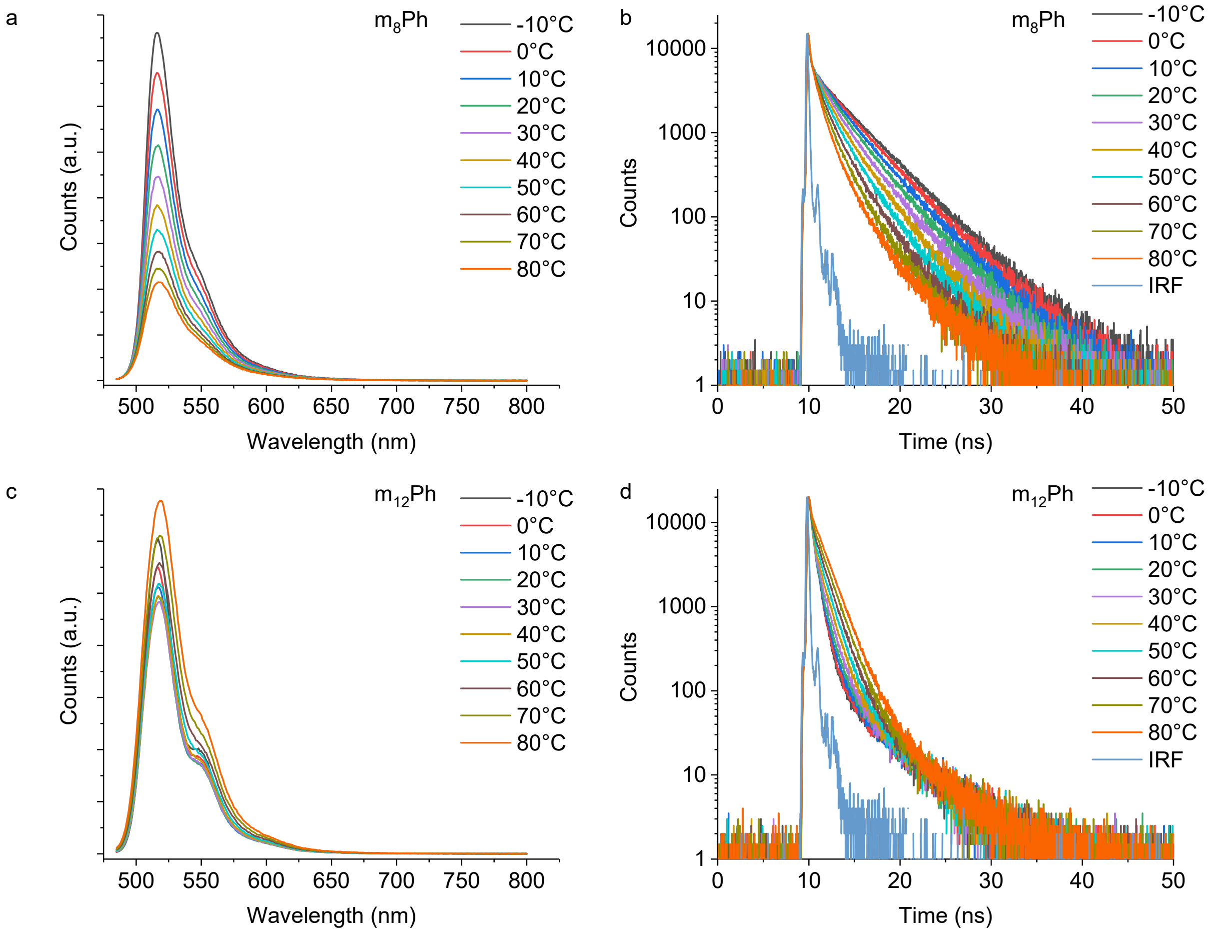

Figure S12. Temperature dependence of fluorescence for m8Ph and m12Ph in DMF from -10 to 80 ºC. (a) and (c) Steady-state spectra upon photoexcitation at λ_{ex} = 490 nm. (b) and (d) Emission lifetime measured at λ_{em} = 520 nm upon photoexcitation at λ_{ex} = 506 nm. IRF = instrument response function.

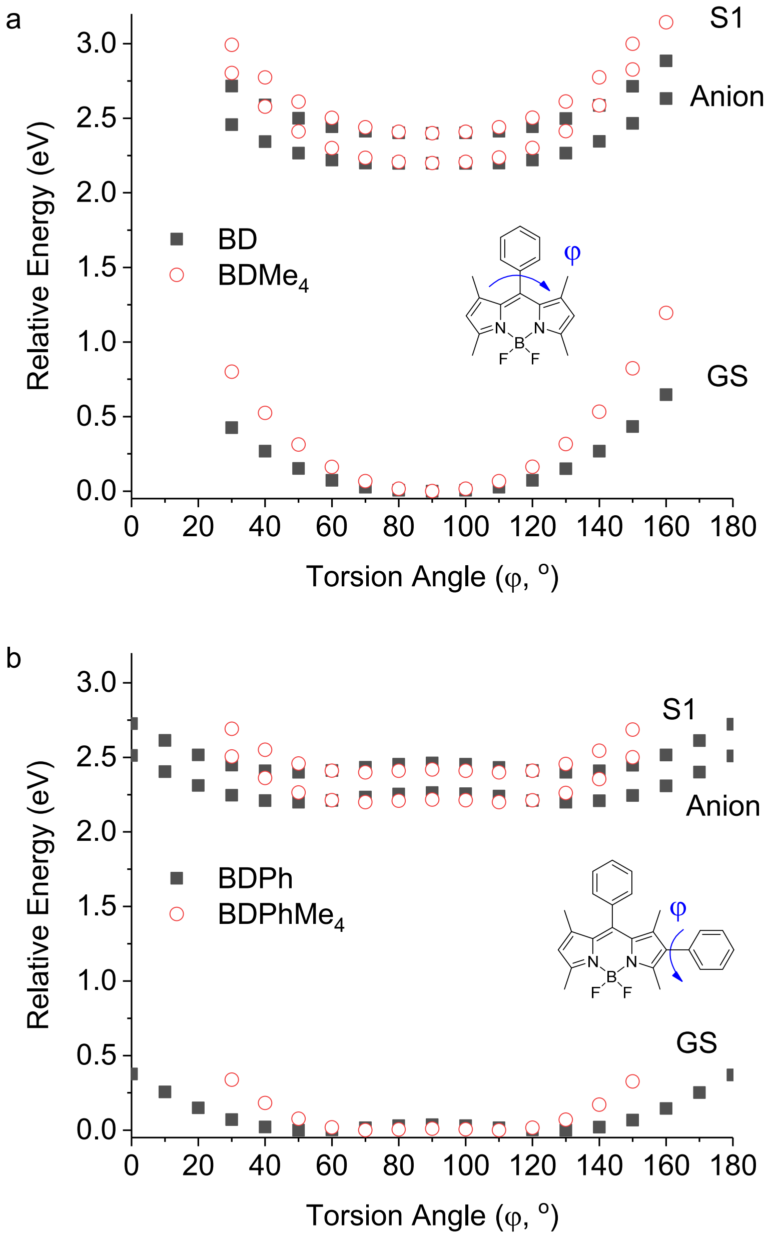

Figure S13. Potential energy surfaces of the singlet excited state (S1), radical anion, and ground state of (a) BD and BDMe$_4$ and (b) BDPh and BDPhMe$_4$ along the torsion angle (*φ*) specified in the figure.

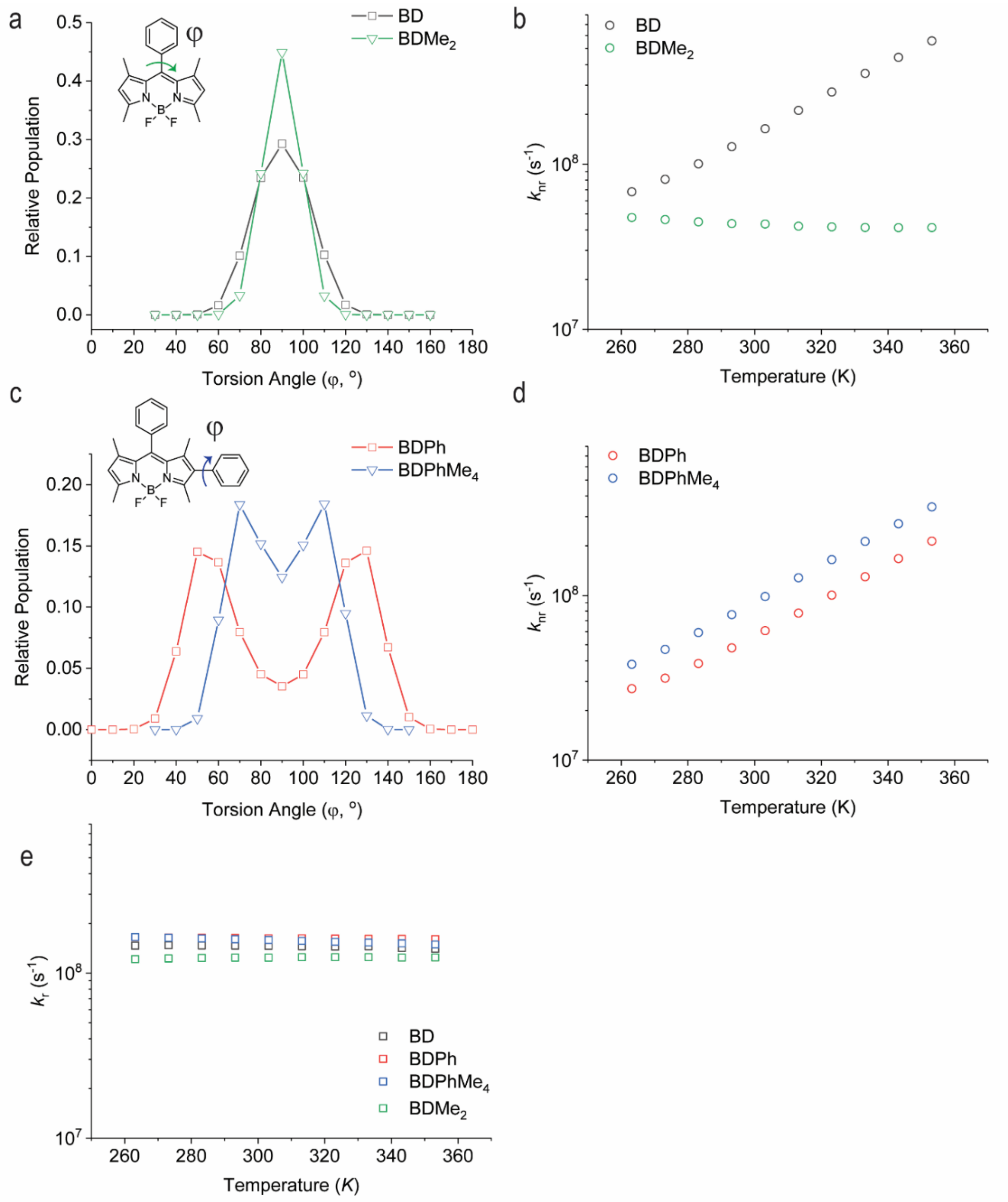

Figure S14. (a) Relative population vs the dihedral angle φ of BD and BDMe$_2$. Relative population was estimated by Boltzmann distribution for 25 ºC. (b) Nonradiative decay constants (k_{nr}) of BD and BDMe$_2$ in DMF over the temperature range of -10 ºC to 80 ºC. (c) Relative population vs the dihedral angle φ of BDPh and BDPhMe$_4$. Relative population was estimated by Boltzmann distribution for 25 ºC. (d) Nonradiative decay constants (k_{nr}) of BDPh and BDPhMe$_4$ over the temperature range of -10 ºC to 80 ºC. (e) Radiative decay constants (k_r) of BD, BDMe$_2$, BDPh and BDPhMe$_4$ over the temperature range of -10 ºC to 80 ºC.

6. Supplementary Tables

Table S1. Reduction Potentials of the β- and *meso*-coupled Dimers and Monomers in MeCN and DCM.[a]

	E^0_{red} (2+/●+, V)		E^1_{red} (●+/0, V)		E^2_{red} (0/●-, V)		E^3_{red} (●-/2-, V)	
Solvent	MeCN	DCM	MeCN	DCM	MeCN	DCM	MeCN	DCM
syn-BD$_2$		0.76		0.73		-1.74		
anti-BD$_2$		0.76		0.74		-1.73		
BD$_2$	0.93		0.75	0.70	-1.49	-1.65	-1.63	-1.79
Ph-BD$_2$		0.79		0.72		-1.65		
m$_{12}$Ph			0.70[b]	0.81	-1.55[b]	-1.68	-1.64[b]	-1.79
m$_8$Ph			0.81	0.81	-1.47	-1.62	-1.50	
BDPhMe$_4$			0.74	0.72	-1.56	-1.73	-2.50	
BDPh	0.85		0.71	0.73	-1.51	-1.67	-2.40	
BD			0.77	0.75	-1.55	-1.69		
BDMe$_2$			0.78	0.75	-1.61	-1.75	-2.66	

[a] Measured with 0.1 M TBA$^+$PF$_6^-$. Reported vs. Fc$^{+/0}$. The error is generally ± 0.02 V. [b] Measured in DMF with 0.1 M TBA$^+$PF$_6^-$.

Table S2. Select Photophysical Properties of the *meso*-coupled BODIPY Dimers and Monomers in Chloroform.

	$\lambda_{\text{abs}}^{\text{max}}$ (nm)	$\lambda_{\text{em}}^{\text{max}}$ (nm)	$\Delta\nu^{a}$ (cm^{-1})	Φ_{em}	τ (ns)	k_{rad} (s^{-1})	k_{nr} (s^{-1})
m_{12}Ph	501	519	692	0.95 ± 0.01	8.9	1.1×10^{8}	5.8×10^{6}
m_8Ph	502	523	800	0.38 ± 0.01	4.2	9.0×10^{7}	1.5×10^{8}
BDMe$_2$	504	514	386	0.95 ± 0.01	4.5	1.7×10^{8}	9.6×10^{6}
BD	502	513	427	0.61 ± 0.02	3.7	1.6×10^{8}	1.1×10^{8}

[a] $\Delta\nu = \nu_{\text{em}}^{\text{max}} - \nu_{\text{abs}}^{\text{max}}$.

Table S3. Select Photophysical Properties of the *meso*-coupled BODIPY Dimers and Monomers in DMF.

	$\lambda_{\mathrm{abs}}^{\mathrm{max}}$ (nm)	$\lambda_{em}^{\mathrm{max}}$ (nm)	$\Delta\nu^{a}$ (cm^{-1})	Φ_{em}	τ (ns)	k_{rad} (s^{-1})	k_{nr} (s^{-1})
m$_{12}$Ph	498	517	738	0.031 ± 0.01	0.36, 1.7	--	--
m$_{8}$Ph	499	515	623	0.027 ± 0.01	0.19, 2.9	--	--
BDMe$_2$	502	515	503	0.74 ^{b}	6.0	1.2×10^{8}	4.4×10^{7}
BD	501	512	349	0.54 ± 0.02	3.6	1.5×10^{8}	1.3×10^{8}

^{a} $\Delta\nu = \nu_{\mathrm{em}}^{\mathrm{max}} - \nu_{\mathrm{abs}}^{\mathrm{max}}$. ^{b} The data taken from ref [39].

Table S4. Total Reorganization (λ), Electronic Coupling (V*), and Activation Energy ($\Delta G^{\ddagger}$) for Symmetry-Breaking Charge Separation.

	λ (eV)	V* (cm^{-1})	$\Delta G^{\ddagger}$ (eV)
m$_{12}$Ph	0.80 ± 0.05	30 ± 3	0.10 ± 0.01
m$_8$Ph	0.60 ± 0.03	27 ± 3	0.064 ± 0.01
syn-BD$_2$	0.52 ± 0.03	14 ± 2	0.060 ± 0.01
Ph-BD$_2$	0.60 ± 0.03	65 ± 3	0.070 ± 0.01

7. Additional References

1. J. T. Buck, A. M. Boudreau, A. DeCarmine, R. W. Wilson, J. Hampsey and T. Mani, Spin-Allowed Transitions Control the Formation of Triplet Excited States in Orthogonal Donor-Acceptor Dyads, *Chem*, 2019, **5**, 138-155.
2. T. Schulte, D. M. Niedzwiedzki, R. R. Birge, R. G. Hiller, T. Polívka, E. Hofmann and H. A. Frank, Identification of a single peridinin sensing Chl-*a* excitation in reconstituted PCP by crystallography and spectroscopy, *Proc. Natl. Acad. Sci. U.S.A.*, 2009, **106**, 20764-20769.
3. I. H. M. van Stokkum, D. S. Larsen and R. van Grondelle, Global and target analysis of time-resolved spectra, *Biochim. Biophys. Acta Bioenerg.*, 2004, **1657**, 82-104.
4. J. Pan, S. Lin, J. P. Allen, J. C. Williams, H. A. Frank and N. W. Woodbury, Carotenoid Excited-State Properties in Photosynthetic Purple Bacterial Reaction Centers: Effects of the Protein Environment, *J. Phys. Chem. B*, 2011, **115**, 7058-7068.
5. M. J. Frisch, G. W. Trucks, H. B. Schlegel, G. E. Scuseria, M. A. Robb, J. R. Cheeseman, G. Scalmani, V. Barone, G. A. Petersson, H. Nakatsuji, X. Li, M. Caricato, A. V. Marenich, J. Bloino, B. G. Janesko, R. Gomperts, B. Mennucci, H. P. Hratchian, J. V. Ortiz, A. F. Izmaylov, J. L. Sonnenberg, Williams, F. Ding, F. Lipparini, F. Egidi, J. Goings, B. Peng, A. Petrone, T. Henderson, D. Ranasinghe, V. G. Zakrzewski, J. Gao, N. Rega, G. Zheng, W. Liang, M. Hada, M. Ehara, K. Toyota, R. Fukuda, J. Hasegawa, M. Ishida, T. Nakajima, Y. Honda, O. Kitao, H. Nakai, T. Vreven, K. Throssell, J. A. Montgomery Jr., J. E. Peralta, F. Ogliaro, M. J. Bearpark, J. J. Heyd, E. N. Brothers, K. N. Kudin, V. N. Staroverov, T. A. Keith, R. Kobayashi, J. Normand, K. Raghavachari, A. P. Rendell, J. C. Burant, S. S. Iyengar, J. Tomasi, M. Cossi, J. M. Millam, M. Klene, C. Adamo, R. Cammi, J. W. Ochterski, R. L. Martin, K. Morokuma, O. Farkas, J. B. Foresman and D. J. Fox, Gaussian 16 Rev. B.01.*Journal*, 2016.
6. A. D. Becke, Density-Functional Thermochemistry. III. The Role of Exact Exchange, *J. Chem. Phys.*, 1993, **98**, 5648-5652.
7. P. J. Stephens, F. J. Devlin, C. F. Chabalowski and M. J. Frisch, Ab-Initio Calculation of Vibrational Absorption and Circular-Dichroism Spectra Using Density-Functional Force-Fields, *J. Phys. Chem.*, 1994, **98**, 11623-11627.
8. J.-D. Chai and M. Head-Gordon, Long-range corrected hybrid density functionals with damped atom-atom dispersion corrections, *Phys. Chem. Chem. Phys.*, 2008, **10**, 6615-6620.
9. L. Estergreen, A. R. Mencke, D. E. Cotton, N. V. Korovina, J. Michl, S. T. Roberts, M. E. Thompson and S. E. Bradforth, Controlling Symmetry Breaking Charge Transfer in BODIPY Pairs, *Accounts Chem. Res.*, 2022, **55**, 1561-1572.
10. R. Improta, G. Scalmani, M. J. Frisch and V. Barone, Toward effective and reliable fluorescence energies in solution by a new state specific polarizable continuum model time dependent density functional theory approach, *J. Chem. Phys.*, 2007, **127**, 074504 074501-074509.
11. R. Improta, V. Barone, G. Scalmani and M. J. Frisch, A state-specific polarizable continuum model time dependent density functional theory method for excited state calculations in solution, *J. Chem. Phys.*, 2006, **125**, 054103 054101-054109.
12. J. Tomasi, B. Mennucci and R. Cammi, Quantum Mechanical Continuum Solvation Models, *Chem. Rev.*, 2005, **105**, 2999-3094.

13. M. Cossi, N. Rega, G. Scalmani and V. Barone, Energies, structures, and electronic properties of molecules in solution with the C-PCM solvation model, *J. Comput. Chem.*, 2003, **24**, 669-681.
14. V. Barone and M. Cossi, Quantum Calculation of Molecular Energies and Energy Gradients in Solution by a Conductor Solvent Model, *J. Phys. Chem. A*, 1998, **102**, 1995-2001.
15. S. E. Koh, C. Risko, D. A. da Silva Filho, O. Kwon, A. Facchetti, J.-L. Brédas, T. J. Marks and M. A. Ratner, Modeling Electron and Hole Transport in Fluoroarene-Oligothiopene Semiconductors: Investigation of Geometric and Electronic Structure Properties, *Adv. Funct. Mater.*, 2008, **18**, 332-340.
16. E. A. B. Kantchev, C. J. O'Brien and M. G. Organ, Palladium Complexes of N-Heterocyclic Carbenes as Catalysts for Cross-Coupling Reactions—A Synthetic Chemist's Perspective, *Angew. Chem. Int. Edit.*, 2007, **46**, 2768-2813.
17. C. J. O'Brien, E. A. B. Kantchev, C. Valente, N. Hadei, G. A. Chass, A. Lough, A. C. Hopkinson and M. G. Organ, Easily Prepared Air- and Moisture-Stable Pd–NHC (NHC=N-Heterocyclic Carbene) Complexes: A Reliable, User-Friendly, Highly Active Palladium Precatalyst for the Suzuki–Miyaura Reaction, *Chem. Eur. J.*, 2006, **12**, 4743-4748.
18. T. E. Barder, S. D. Walker, J. R. Martinelli and S. L. Buchwald, Catalysts for Suzuki−Miyaura Coupling Processes: Scope and Studies of the Effect of Ligand Structure, *J. Am. Chem. Soc.*, 2005, **127**, 4685-4696.
19. Z. Li, Y. Liu, X. Hou, Z. Xu, C. Liu, F. Zhang and Z. Xie, The crystal structures, spectrometric, photodynamic properties and bioimaging of β-β linked Bodipy oligomers, *J. Lumin.*, 2019, **212**, 306-314.
20. J. Fan, S. Willdorf-Cohen, E. M. Schibli, Z. Paula, W. Li, T. J. G. Skalski, A. T. Sergeenko, A. Hohenadel, B. J. Frisken, E. Magliocca, W. E. Mustain, C. E. Diesendruck, D. R. Dekel and S. Holdcroft, Poly(bis-arylimidazoliums) possessing high hydroxide ion exchange capacity and high alkaline stability, *Nat. Commun.*, 2019, **10**, 2306.
21. R. Gotor, A. M. Costero, P. Gaviña and S. Gil, Ratiometric double channel borondipyrromethene based chemodosimeter for the selective detection of nerve agent mimics, *Dyes Pigm.*, 2014, **108**, 76-83.
22. H. Sunahara, Y. Urano, H. Kojima and T. Nagano, Design and Synthesis of a Library of BODIPY-Based Environmental Polarity Sensors Utilizing Photoinduced Electron-Transfer-Controlled Fluorescence ON/OFF Switching, *J. Am. Chem. Soc.*, 2007, **129**, 5597-5604.
23. A. Osuka, G. Noya, S. Taniguchi, T. Okada, Y. Nishimura, I. Yamazaki and N. Mataga, Energy-Gap Dependence of Photoinduced Charge Separation and Subsequent Charge Recombination in 1,4-Phenylene-Bridged Zinc-Free-Base Hybrid Porphyrins, *Chem. Eur. J.*, 2000, **6**, 33-46.
24. S. Chaudhuri, S. Hedström, D. D. Méndez-Hernández, H. P. Hendrickson, K. A. Jung, J. Ho and V. S. Batista, Electron Transfer Assisted by Vibronic Coupling from Multiple Modes, *J. Chem. Theory Comput.*, 2017, **13**, 6000-6009.
25. A. V. Marenich, C. J. Cramer and D. G. Truhlar, Universal Solvation Model Based on Solute Electron Density and on a Continuum Model of the Solvent Defined by the Bulk

Dielectric Constant and Atomic Surface Tensions, *J. Phys. Chem. B*, 2009, **113**, 6378-6396.

26. P. Vath and M. B. Zimmt, A Spectroscopic Study of Solvent Reorganization Energy: Dependence on Temperature, Charge Transfer Distance, and the Type of Solute−Solvent Interactions, *J. Phys. Chem. A*, 2000, **104**, 2626-2633.
27. S. Johnson, A. Makhijani, M. Tsuji and T. Mani, Acceleration of Nonradiative Charge Recombination Reactions at Larger Distances in Kinked Donor–Bridge–Acceptor Molecules, *J. Phys. Chem. B*, 2022, **126**, 8851-8863.
28. J. T. Buck and T. Mani, Magnetic Control of Recombination Fluorescence and Tunability by Modulation of Radical Pair Energies in Rigid Donor–Bridge–Acceptor Systems, *J. Am. Chem. Soc.*, 2020, **142**, 20691-20700.
29. J. T. Buck, R. W. Wilson and T. Mani, Intramolecular Long-Range Charge-Transfer Emission in Donor–Bridge–Acceptor Systems, *J. Phys. Chem. Lett.*, 2019, **10**, 3080-3086.
30. A. C. Benniston, G. Copley, A. Harriman, D. Howgego, R. W. Harrington and W. Clegg, Cofacial Boron Dipyrromethene (Bodipy) Dimers: Synthesis, Charge Delocalization, and Exciton Coupling, *J. Org. Chem.*, 2010, **75**, 2018-2027.
31. A. Takai, C. P. Gros, J.-M. Barbe, R. Guilard and S. Fukuzumi, Enhanced Electron-Transfer Properties of Cofacial Porphyrin Dimers through π–π Interactions, *Chem. Eur. J.*, 2009, **15**, 3110-3122.
32. N. Elgrishi, K. J. Rountree, B. D. McCarthy, E. S. Rountree, T. T. Eisenhart and J. L. Dempsey, A Practical Beginner's Guide to Cyclic Voltammetry, *J. Chem. Educ.*, 2018, **95**, 197-206.
33. T. Mani, D. C. Grills, M. D. Newton and J. R. Miller, Electron Localization of Anions Probed by Nitrile Vibrations, *J. Am. Chem. Soc.*, 2015, **137**, 10979-10991.
34. D. H. Evans, One-Electron and Two-Electron Transfers in Electrochemistry and Homogeneous Solution Reactions, *Chem. Rev.*, 2008, **108**, 2113-2144.
35. T. Mani, D. C. Grills and J. R. Miller, Vibrational Stark Effects to Identify Ion Pairing and Determine Reduction Potentials in Electrolyte-Free Environments, *J. Am. Chem. Soc.*, 2015, **137**, 1136-1140.
36. J. Hack, D. C. Grills, J. R. Miller and T. Mani, Identification of Ion-Pair Structures in Solution by Vibrational Stark Effects, *J. Phys. Chem. B*, 2016, **120**, 1149-1157.
37. N. K. Lee, S. Park, M.-H. Yoon, Z. H. Kim and S. K. Kim, Effect of ring torsion on intramolecular vibrational redistribution dynamics of 1,1′-binaphthyl and 2,2′-binaphthyl, *Phys. Chem. Chem. Phys.*, 2012, **14**, 840-848.
38. H. M. McConnell, Intramolecular Charge Transfer in Aromatic Free Radicals, *J. Chem. Phys.*, 1961, **35**, 508-515.
39. G. Meng, S. Velayudham, A. Smith, R. Luck and H. Liu, Color Tuning of Polyfluorene Emission with BODIPY Monomers, *Macromolecules*, 2009, **42**, 1995-2001.

Syn-BD2 1H Spectrum in CDCl3

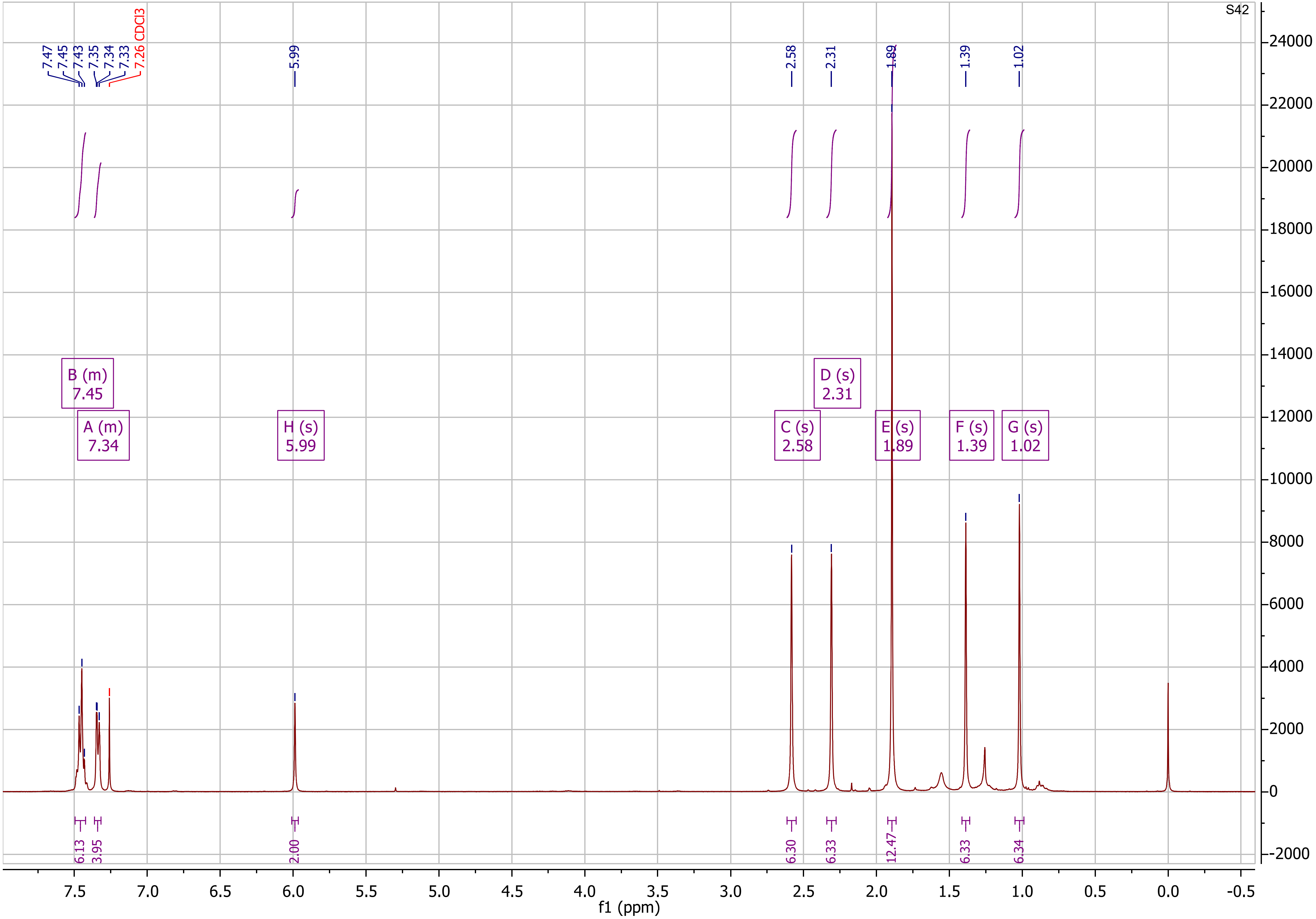

Syn-BD2 13C NMR Spectrum in CDCl3

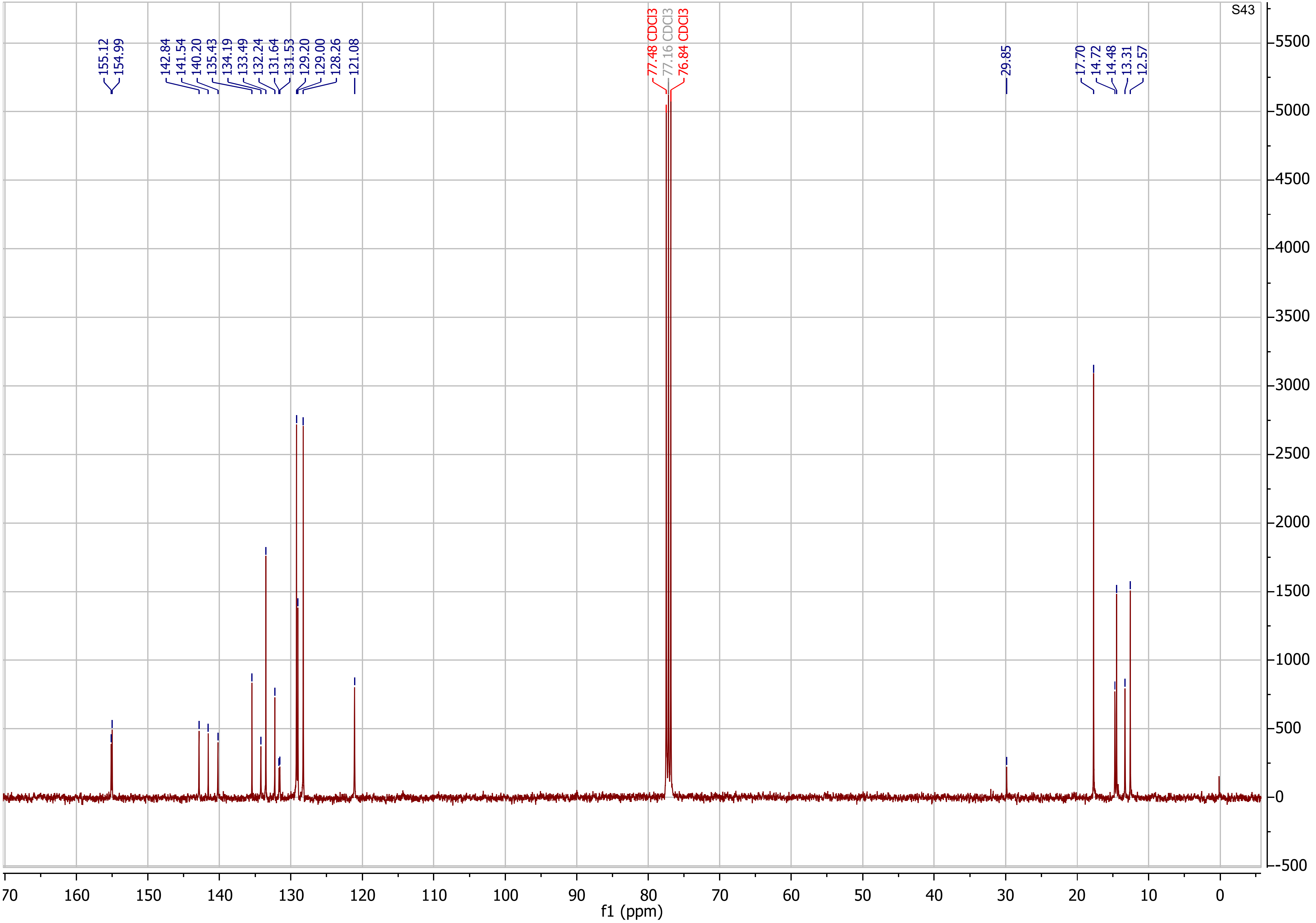

Anti-BD2 1H Spectrum in CDCl3

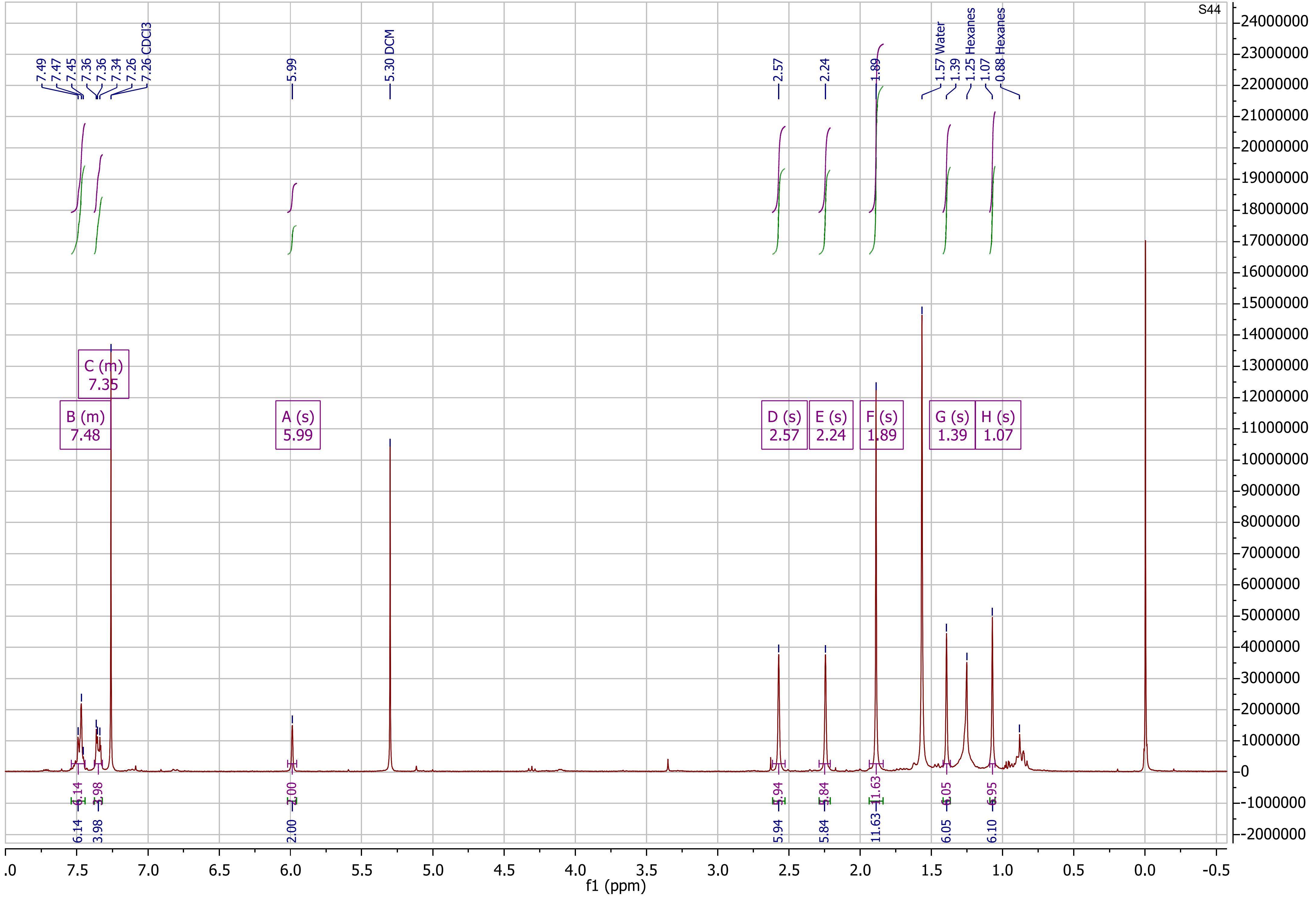

Anti-BD2 13C NMR Spectrum in CDCl3

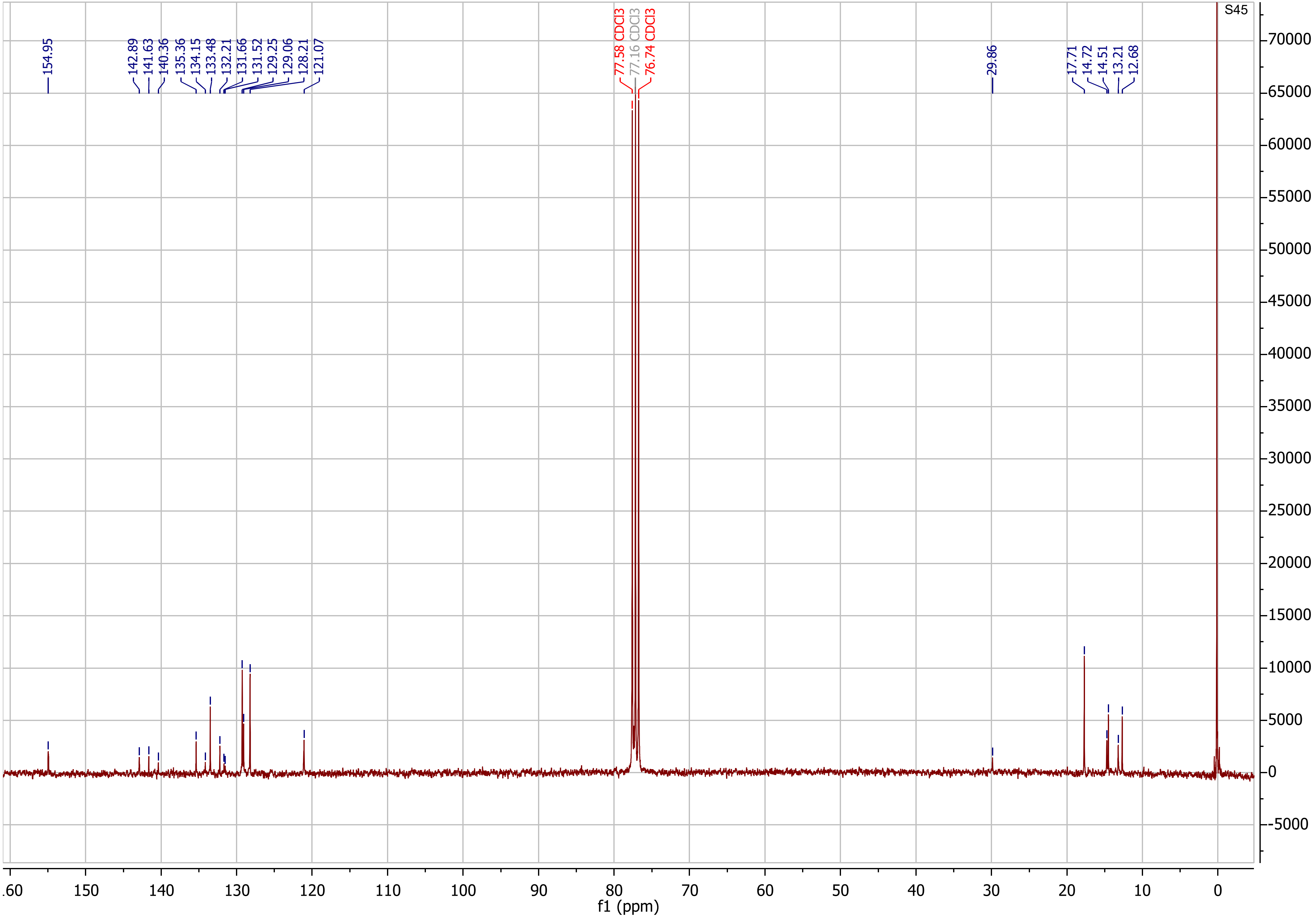

Ph-BD2 1H Spectrum in CD2Cl2

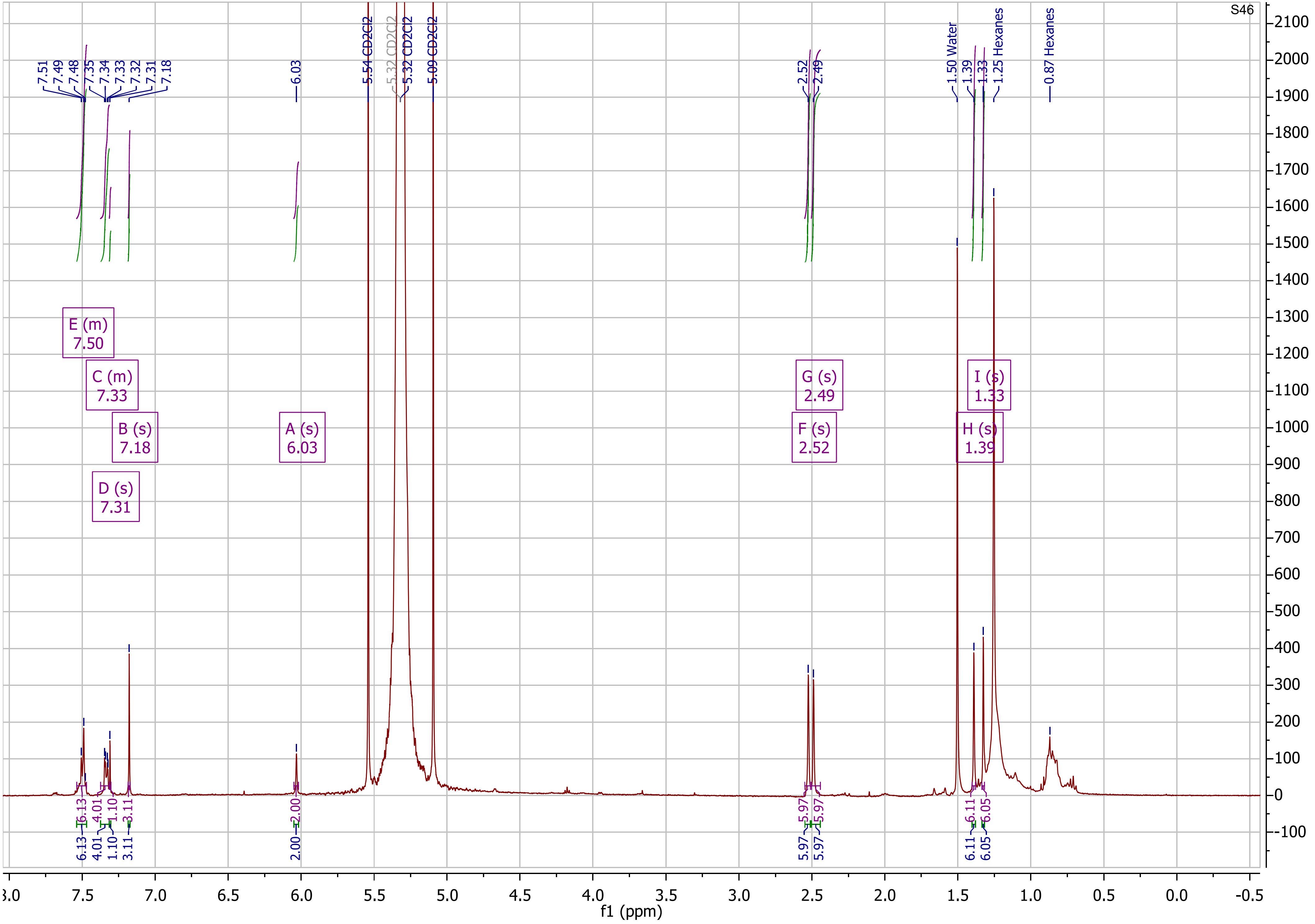

BDPhMe4 1H Spectrum in CDCl3

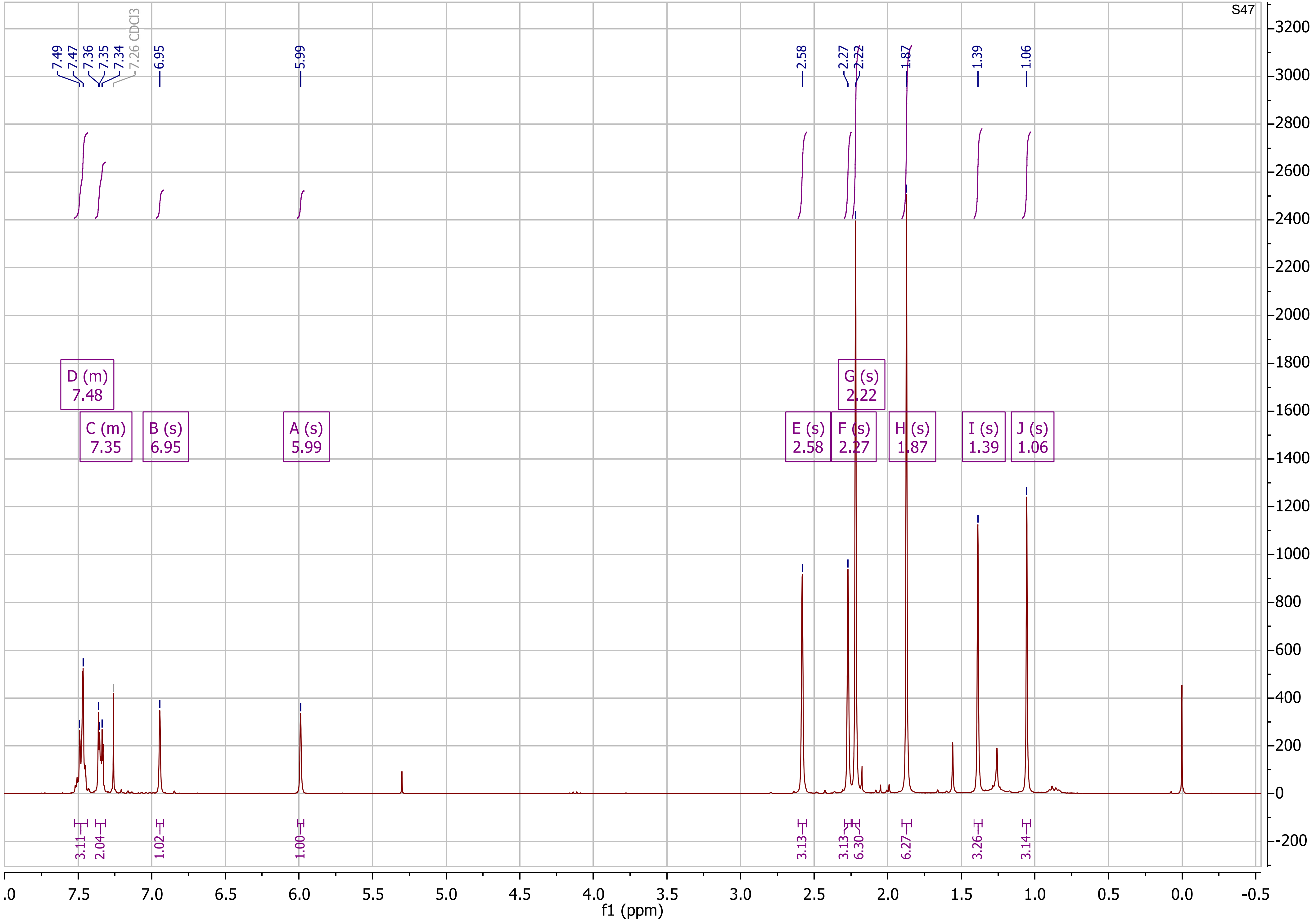

BDPhMe4 13C Spectrum in CDCl3

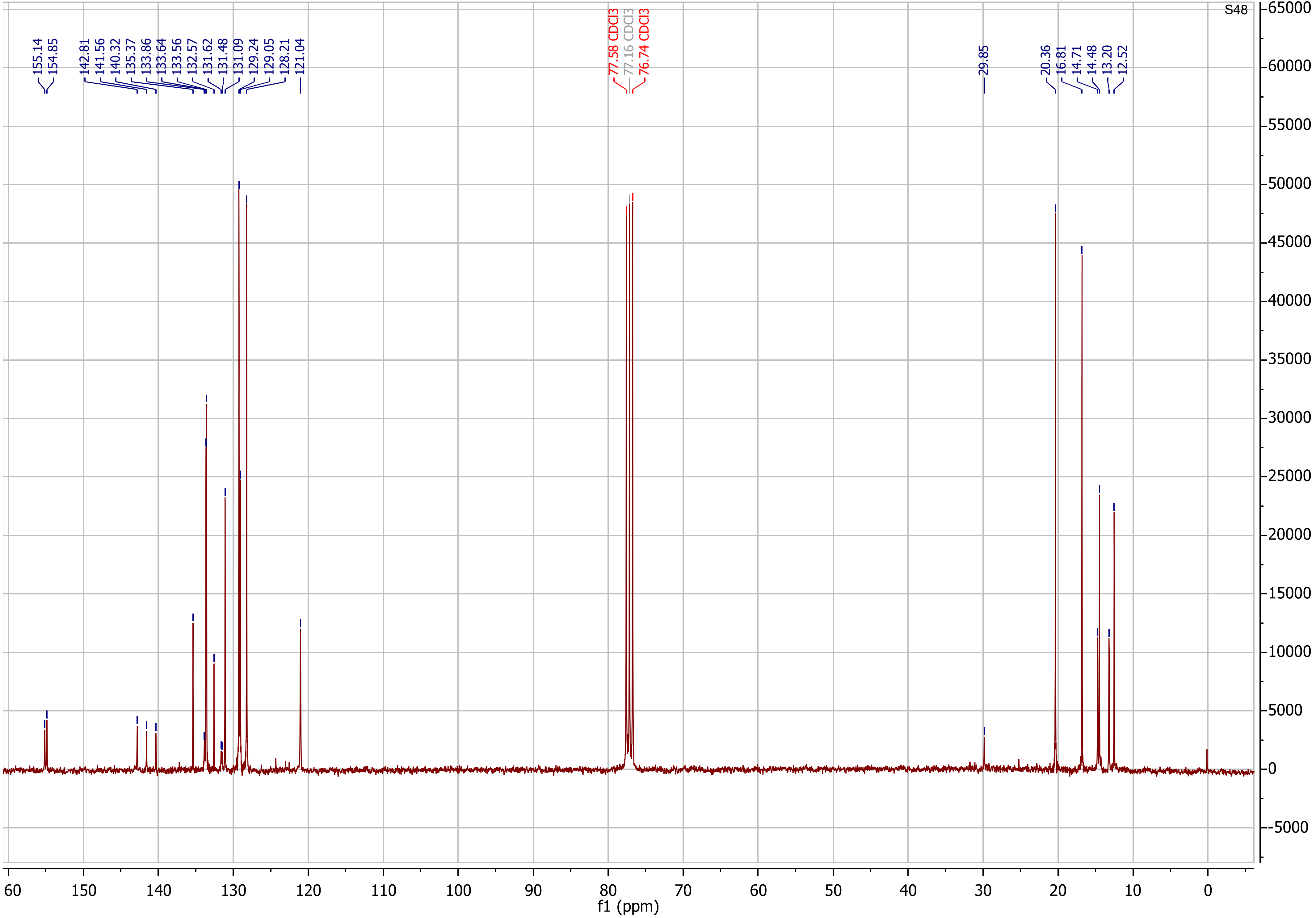

BDPh 1H NMR Spectrum in CDCl3

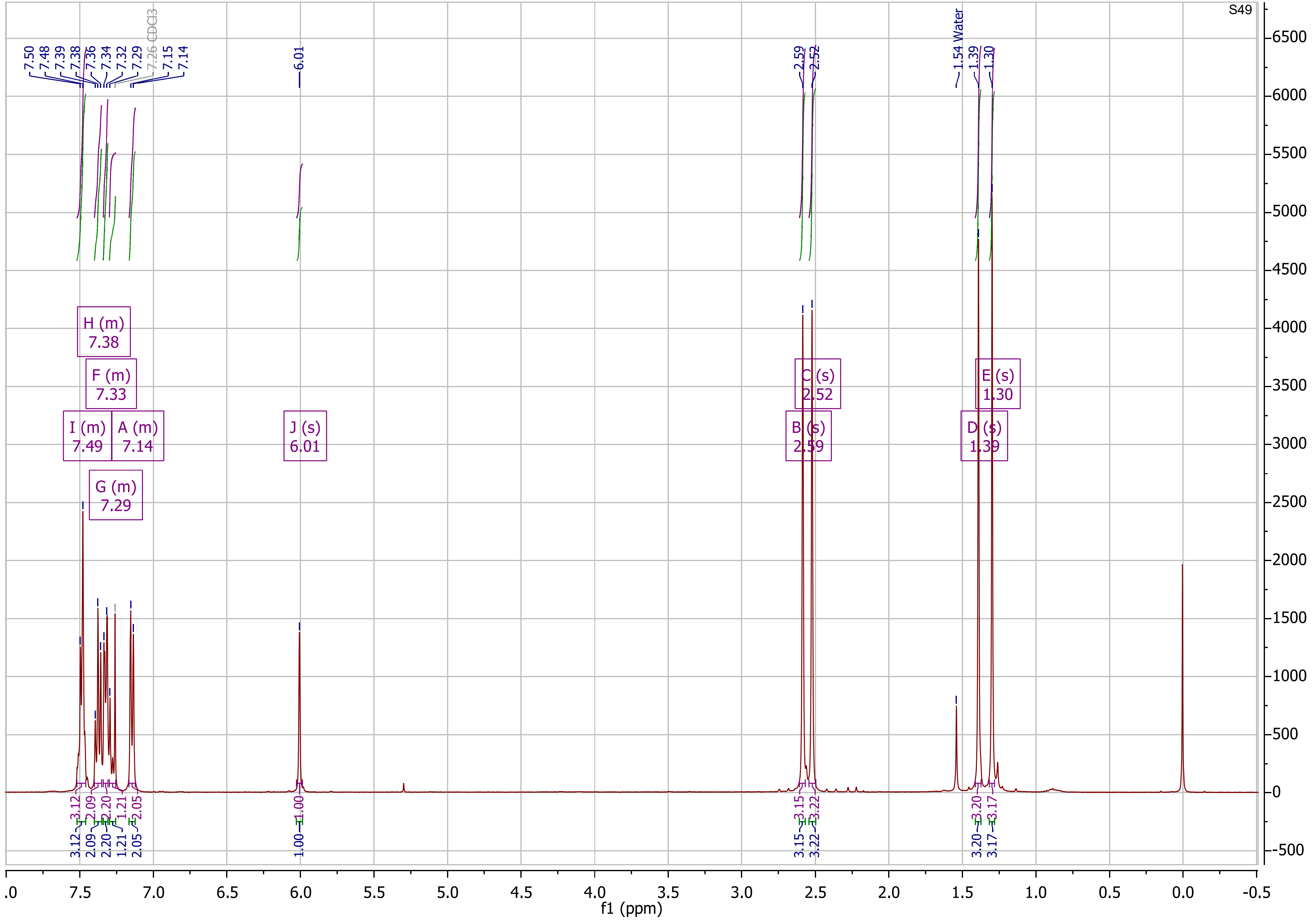

BDPh 13C NMR Spectraum in CDCl3

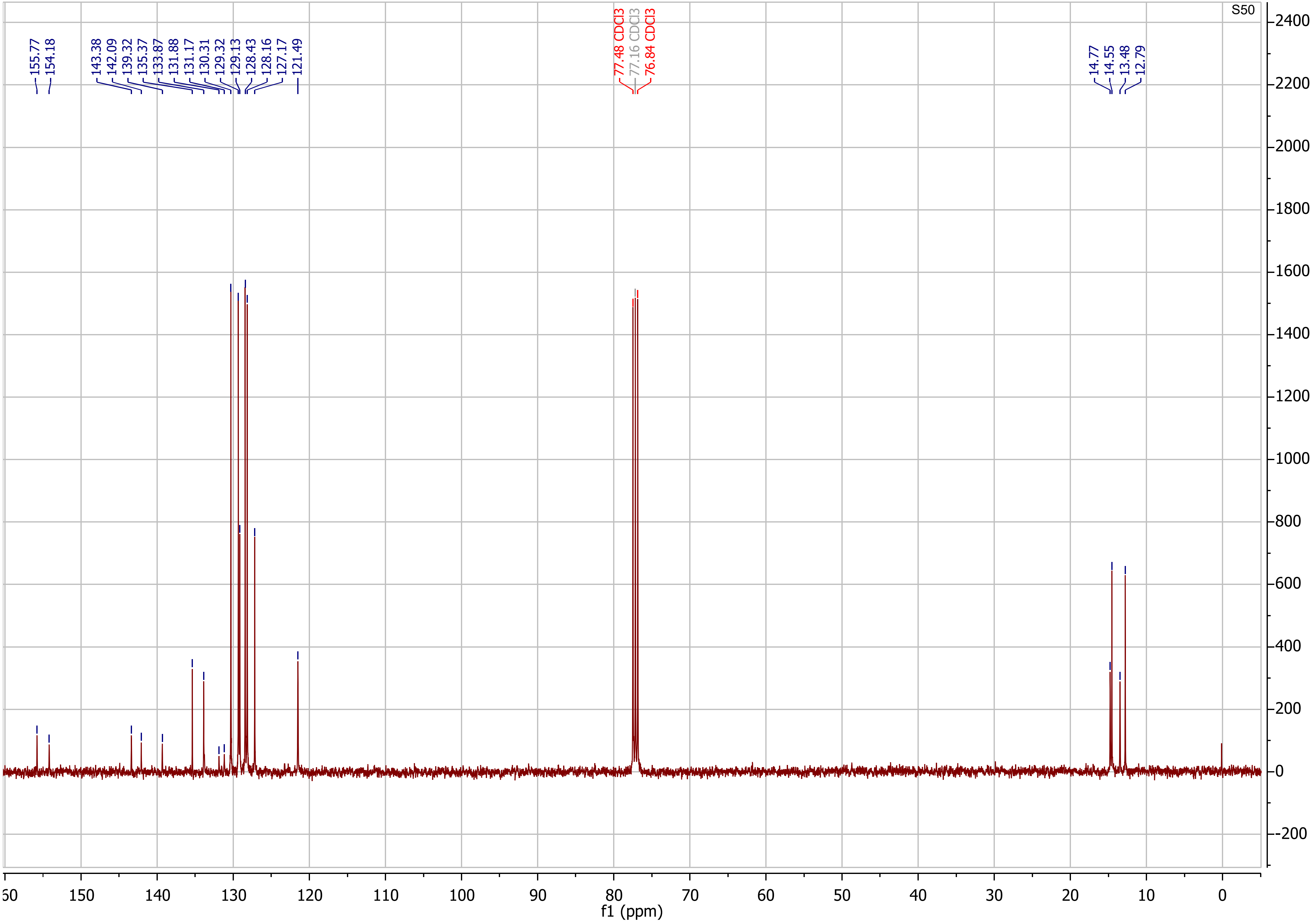

PhMe4Bpin 1H Spectrum in CDCl3

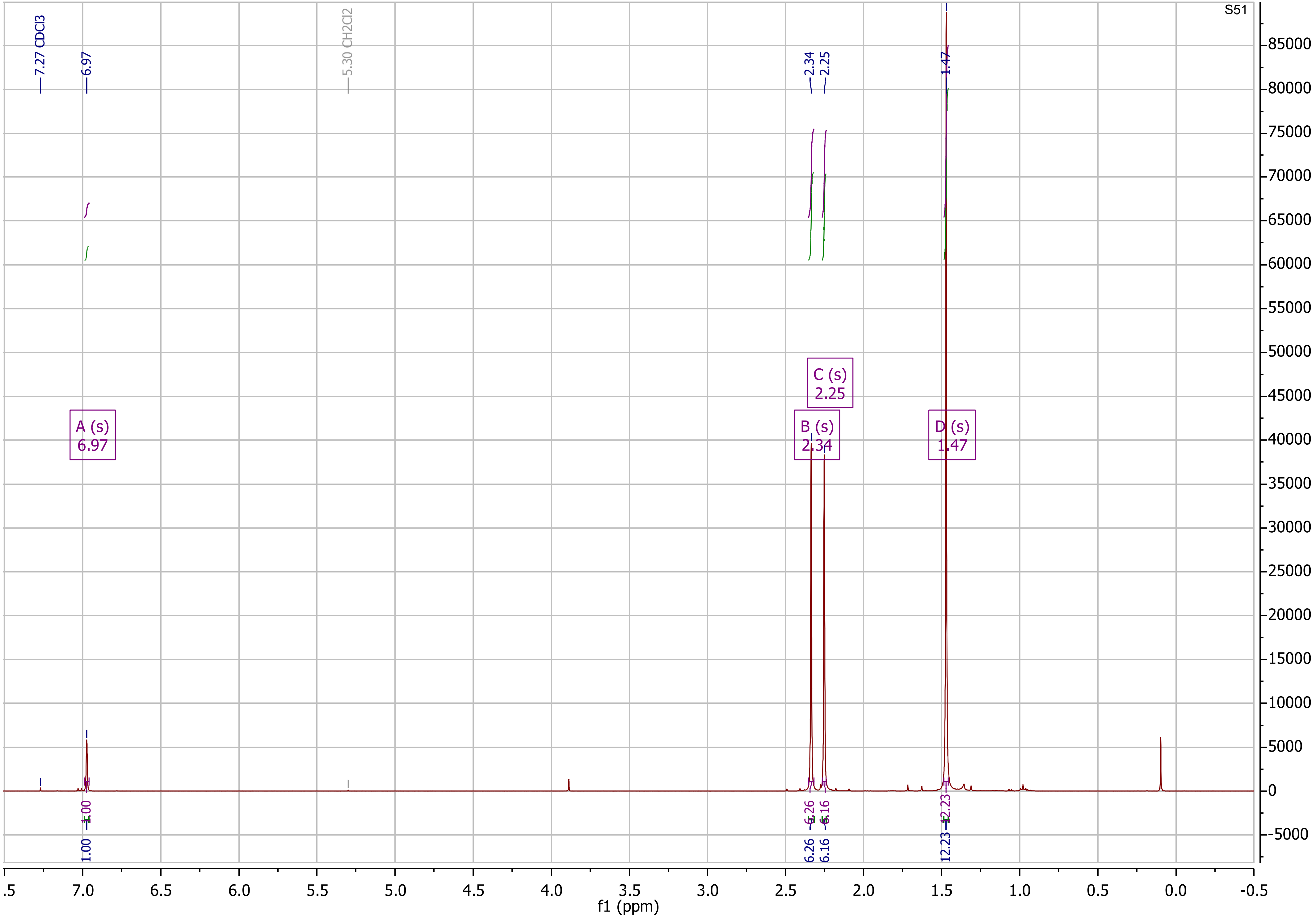

BDBpin 1H Spectrum in CDCl3

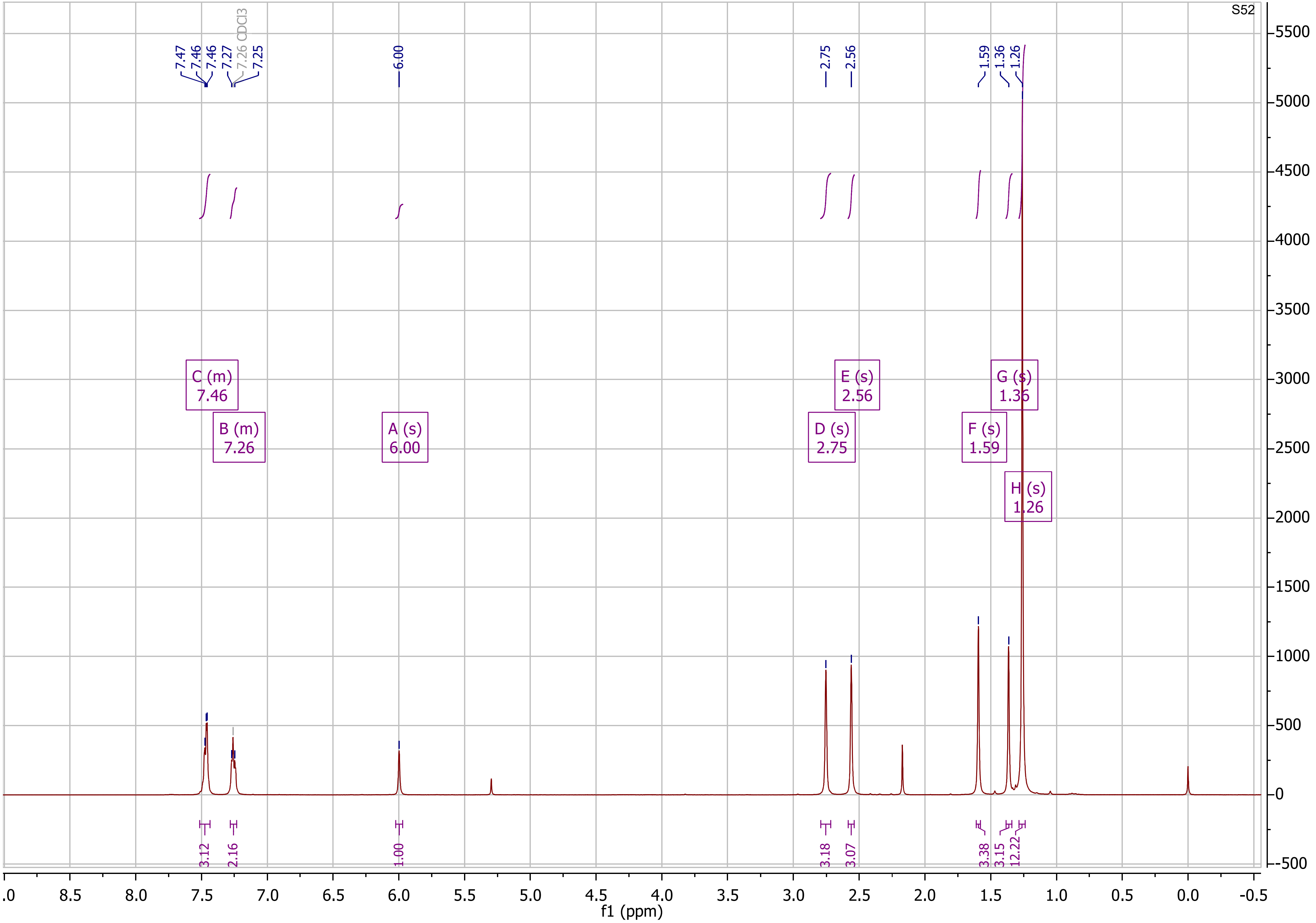

BDBpin 13C Spectrum in CDCl3

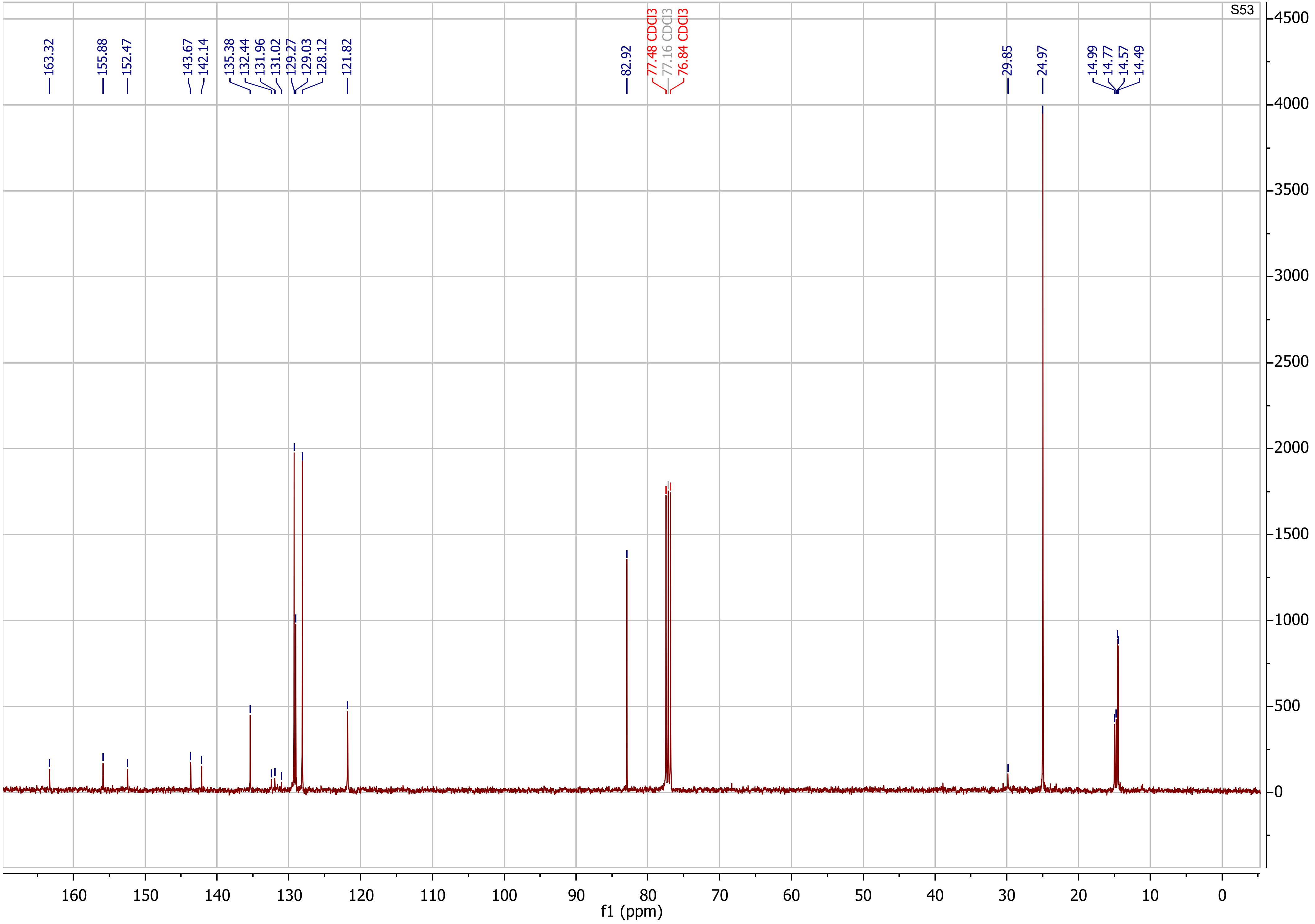

m12Ph 1H Spectrum in CDCl3